Available online at www.sciencedirect.com
SCIENCE DIRECT®
ELSEVIER
Nuclear Instruments and Methods in Physics Research A 522 (2004) 294–346
NUCLEAR INSTRUMENTS & METHODS IN PHYSICS RESEARCH Section A
www.elsevier.com/locate/nima

Basic instrumentation for Hall A at Jefferson Lab

J. Alcorn[a], B.D. Anderson[b], K.A. Aniol[c], J.R.M. Annand[d], L. Auerbach[e], J. Arrington[f], T. Averett[g], F.T. Baker[h], M. Baylac[a,i], E.J. Beise[j], J. Berthot[k], P.Y. Bertin[k], W. Bertozzi[l], L. Bimbot[m], T. Black[l,1], W.U. Boeglin[n], D.V. Boykin[o], E.J. Brash[p], V. Breton[k], H. Breuer[j], P. Brindza[a], D. Brown[j], E. Burtin[i], J.R. Calarco[o], L.S. Cardman[a], R. Carr[q], G.D. Cates[r,s], C. Cavata[i], Z. Chai[l], C.C. Chang[j], N.S. Chant[j], J.-P. Chen[a], S. Choi[e], E. Chudakov[a], S. Churchwell[t], M. Coman[n], E. Cisbani[u], S. Colilli[u], N. Colombel[i,s], R. Crateri[u], D.S. Dale[v], N. Degrande[w], C.W. de Jager[a,*], R. De Leo[x], A. Deur[a,k,s], G. Dezern[a], B. Diederich[y], S. Dieterich[z], R. di Salvo[k], P. Djawotho[g], J. Domingo[a], J.-E. Ducret[i], D. Dutta[l,t], K. Egiyan[aa], M.B. Epstein[c], S. Escoffier[i], S. Esp[a], L.A. Ewell[j], J.M. Finn[g], K.G. Fissum[l,ab], E. Folts[a], H. Fonvieille[k], B. Frois[i], S. Frullani[u], H. Gao[l,t], J. Gao[l,q], F. Garibaldi[u], A. Gasparian[v,ac], A. Gavalya[a], O. Gayou[g,l], S. Gilad[l], R. Gilman[a,z], F. Giuliani[u], A. Glamazdin[ad], C. Glashausser[z], J. Gomez[a], V. Gorbenko[ad], T. Gorringe[v], M. Gricia[u], K. Griffioen[g], D. Hamilton[d], J.-O. Hansen[a], F.W. Hersman[o], D.W. Higinbotham[a], R. Holmes[ae], H. Holmgren[j], M. Holtrop[o], N. d'Hose[i], E. Hovhannisyan[aa], C. Howell[t], G.M. Huber[p], E. Hughes[q], C.E. Hyde-Wright[y], H. Ibrahim[y], S. Incerti[e], M. Iodice[af], R. Iommi[u], D. Ireland[d], S. Jaminion[k], J. Jardillier[i], S. Jensen[q], X. Jiang[z], C.E. Jones[q], M.K. Jones[a,g], K. Joo[s,2], C. Jutier[k,y], W. Kahl[ae], S. Kato[ag], A.T. Katramatou[b], J.J. Kelly[ad], S. Kerhoas[i], A. Ketikyan[aa], M. Khandaker[ah], M. Khayat[b], K. Kino[ai], I. Kominis[r], W. Korsch[v], S. Kox[ai], K. Kramer[g], K.S. Kumar[r,ak], G. Kumbartzki[z], M. Kuss[a], L. Lagamba[x], G. Laveissière[k], A. Leone[al], J.J. LeRose[a], F. Marie[i], L. Levchuk[ad], M. Leuschner[o], D. Lhuillier[i], M. Liang[a], K. Livingston[d], R.A. Lindgren[s], N. Liyanage[a,l,s], G.J. Lolos[s], R.W. Lourie[am,an], M. Lucentini[u], R. Madey[a,b,ac], K. Maeda[ai], S. Malov[z], D.M. Manley[b], D.J. Margaziotis[c], P. Markowitz[n], J. Marroncle[i], J. Martine[i], S. Mayilyan[aa], J.S. McCarthy[s], K. McCormick[b,y,z], J. Mclntyre[z],

*Corresponding author. Tel.: +1-757-269-5254; fax: +1-757-269-5703.
E-mail address: kees@jlab.org (C.W. de Jager).
[1] Present address: Dartmouth College, Hanover, NH 03755, USA
[2] Present address: University of Connecticut, Storrs, CT 06269, USA.

0168-9002/$ - see front matter
doi:10.1016/j.nima.2003.11.415

R.D. McKeown[q], D. Meekins[a], R.L.J. van der Meer[a,p], Z.-E. Meziani[e], R. Michaels[a], B. Milbrath[ao], J.A. Miller[a], W. Miller[r], J. Mitchell[a,an], J. Mougey[aj], S. Nanda[a], A. Nathan[ap], D. Neyret[i], E.A.J.M. Offermann[a,an], Z. Papandreou[p], C.F. Perdrisat[g], R. Perrino[al], G.G. Petratos[b], A. Petrosyan[aa], L. Pierangeli[u], S. Platchkov[i], R. Pomatsalyuk[ad], D. Pripstein[q], D.L. Prout[b], V.A. Punjabi[ah], T. Pussieux[i], G. Quéméner[g,k], R.D. Ransomez[z], O. Ravel[k], B. Reitz[a], Y. Roblin[a,k], R. Roche[aq,y], M. Roedelbronn[ap], O.A. Rondon-Aramayo[s], P.G. Roos[j], G. Rosner[d], D. Rowntree[l], G.A. Rutledge[g], P.M. Rutt[a], M. Rvachev[l], F. Sabatavenere[i,y], A. Saha[a], T. Saito[ai], F. Santavenere[u], A.J. Sarty[aq,ar], W.J. Schneider[a], J.P. Segal[a], A. Serdarevic-Offermann[a,p], A. Shahinyan[aa], K. Slifer[e], T.P. Smith[o], A. Soldi[as], P. Sorokin[ad], P. Souder[ae], S.L. Spiegel[a], M.A. Stevens[a], S. Strauch[z,3], R. Suleiman[b,l], J.A. Templon[h,4], T. Terasawa[ai], L. Todor[y,5], H. Tsubota[ai], H. Ueno[ag], P.E. Ulmer[y], G.M. Urciuoli[u], L. Van Hoorebeke[w], R. Van de Vyver[w], S. van Verst[l], P. Vernin[i], B. Vlahovic[a,as], H. Voskanyan[aa], E. Voutier[aj], R. Walter[t], J.W. Watson[b], D.P. Watts[d], L.B. Weinstein[y], K. Wijesooriya[f,g,t], B. Wojtsekhowski[a], H. Xiang[l], F. Xiong[l], W. Xu[l], D.G. Zainea[p], V. Zeps[v], J. Zhao[l], X. Zheng[f,1], Z.-L. Zhou[l], L. Zhu[l], P.A. Zolnierczuk[v]

[a] *Thomas Jefferson National Accelerator Facility, Newport News, VA 23606, USA*
[b] *Kent State University, Kent, OH 44242, USA*
[c] *California State University Los Angeles, Los Angeles, CA 90032, USA*
[d] *University of Glasgow, Glasgow G12 8QQ, Scotland, UK*
[e] *Temple University, Philadelphia, PA 19122, USA*
[f] *Argonne National Lab, Argonne, IL 60439, USA*
[g] *College of William and Mary, Williamsburg, VA 23187, USA*
[h] *University of Georgia, Athens, GA 30602, USA*
[i] *CEA Saclay, F-91191 Gif-sur-Yvette, France*
[j] *University of Maryland, College Park, MD 20742, USA*
[k] *Université Blaise Pascal/IN2P3, F-63177 Aubière, France*
[l] *Massachusetts Institute of Technology, Cambridge, MA 02139, USA*
[m] *Institut de Physique Nucléaire, F-91406 Orsay, France*
[n] *Florida International University, Miami, FL 33199, USA*
[o] *University of New Hampshire, Durham, NH 03824, USA*
[p] *University of Regina, Regina, Sask., Canada, S4S OA2*
[q] *California Institute of Technology, Pasadena, CA 91125, USA*
[r] *Princeton University, Princeton, NJ 08544, USA*
[s] *University of Virginia,Charlottesville, VA 22901, USA*
[t] *Duke University, Durham, NC 27706, USA*
[u] *INFN, Sezione Sanitá and Istituto Superiore di Sanitá, Laboratorio di Fisica, I-00161 Rome, Italy*
[v] *University of Kentucky, Lexington, KY 40506, USA*
[w] *Gent State University, Nuclear Physics Lab, B-9000 Gent, Belgium*
[x] *INFN, Sezione di Bari and University of Bari, I-70126 Bari, Italy*
[y] *Old Dominion University, Norfolk, VA 23529, USA*

[3] Present address: George Washington University, Washington, DC 20052, USA.
[4] Present address: NIKHEF, Amsterdam, The Netherlands.
[5] Present address: Carnegie Mellon University, Pittsburgh, PA 15217, USA.

[z] Rutgers, The State University of New Jersey, Piscataway, NJ 08854, USA
[aa] Yerevan Physics Institute, Yerevan 375036, Armenia
[ab] University of Lund, Box 118, SE-221 00 Lund, Sweden
[ac] Hampton University, Hampton, VA 23668, USA
[ad] Kharkov Institute of Physics and Technology, Kharkov 61108, Ukraine
[ae] Syracuse University, Syracuse, NY 13244, USA
[af] INFN, Sezione di Roma III, I-00146 Roma, Italy
[ag] Yamagata University, Yamagata, 990, Japan
[ah] Norfolk State University, Norfoik, VA 23504, USA
[ai] Tohoku University, Sendai 980, Japan
[aj] Laboratoire de Physique Subatomique et de Cosmologie, F-38026 Grenoble, France
[ak] University of Massachusetts, Amherst, MA 01003, USA
[al] INFN, Sezione di Lecce, 1-73100 Lecce, Italy
[am] State University of New York at Stony Brook, Stony Brook, NY 11794, USA
[an] Renaissance Technologies Corp., Setauket, NY 11733, USA
[ao] Eastern Kentucky University, Richmond, KY 40475, USA
[ap] University of Illinois, Urbana, IL 61801, USA
[aq] Florida State University, Tallahassee, FL 32306, USA
[ar] Saint Mary's University, Halifax, NS, Canada B3H 3C3
[as] North Carolina Central University, Durham, NC 27707, USA

Received 16 July 2003; received in revised form 7 November 2003; accepted 17 November 2003

Abstract

The instrumentation in Hall A at the Thomas Jefferson National Accelerator Facility was designed to study electro- and photo-induced reactions at very high luminosity and good momentum and angular resolution for at least one of the reaction products. The central components of Hall A are two identical high resolution spectrometers, which allow the vertical drift chambers in the focal plane to provide a momentum resolution of better than 2×10^{-4}. A variety of Cherenkov counters, scintillators and lead-glass calorimeters provide excellent particle identification. The facility has been operated successfully at a luminosity well in excess of 10^{38} cm^{-2} s^{-1}. The research program is aimed at a variety of subjects, including nucleon structure functions, nucleon form factors and properties of the nuclear medium.

PACS: 28.41.Rc; 29.30. − h; 25.20. − x

Keywords: Jefferson Lab; Hall A; Instrumentation

1. Introduction

The scientific goal of the Continuous Electron Beam Accelerator Facility (CEBAF) at Jefferson Lab (JLab) is to investigate the structure of nuclei and hadrons and the underlying fundamental interactions in the region below the high-energy "asymptotically free" regime. In this region several concepts are used: on the one hand, nucleons and mesons are considered the appropriate degrees of freedom in nuclei. On the other hand, the success of current models is limited. For example, the structure of the deuteron is not fully understood at distances smaller than 1.5 fm. Mesonic degrees of freedom are known to be important in the electromagnetic interaction, yet pionic ones are absent from the dynamics. The role of quark degrees of freedom in nuclei remains elusive. The nucleon structure itself is beset with conceptual difficulties in connecting constituent quark models with the underlying QCD Lagrangian which is known to work well in the high-energy perturbative QCD regime. CEBAF's 5.7 GeV, continuous-wave electron beam is, in many respects, an ideal

probe for the study of this strong QCD region because the electromagnetic interaction is well understood, and the wavelength of the electron at this energy is a few percent of the nucleon's size. The availability of polarized electron beams extends the capabilities of the facility to include both spin-dependent interactions and parity-violation experiments, which probe, respectively, the spin and the weak neutral current structures of the system under study.

CEBAF [1] (see Fig. 1) was originally designed to accelerate electrons up to 4 GeV by recirculating the beam up to four times through two superconducting linacs, each producing an energy gain of 400 MeV per pass. Electrons can be injected into the accelerator from either a thermionic or a polarized gun. In the polarized gun a strained GaAs cathode is illuminated by a 1497 MHz gain-switched diode laser, operated at 780 nm. The polarization is measured at the injector with a 5 MeV Mott polarimeter and the polarization vector can be oriented with a Wien filter. The current to the three experimental Halls A, B and C can be controlled independently. Each linac contains 20 cryomodules with a design accelerating gradient of 5 MeV/m. Ongoing in situ processing has already resulted in an average gradient in excess of 7 MeV/m, which has made it possible to accelerate electrons to 5.7 GeV. The design maximum current is 200 μA CW, which can be split arbitrarily between three interleaved 499 MHz bunch trains. One such bunch train can be peeled off after each linac pass to any one of the Halls using RF separators and septa. All Halls can simultaneously receive the maximum energy beam. Hall B with its CEBAF Large Acceptance Spectrometer (CLAS) [2] requires a current as low as 1 nA, while a 100 μA beam is being delivered to one or even both of the other Halls. Hall C has been operational since November 1995, Hall A since May 1997 and Hall B since December 1997.

The basic layout of Hall A is shown in Fig. 2. The central elements are the two High Resolution Spectrometers (HRS). Both of these devices provide a momentum resolution of better than 2×10^{-4} and a horizontal angular resolution of better than 2 mrad at a design maximum central momentum of 4 GeV/c. The present base instrumentation in Hall A has been used with great success for experiments which require high luminosity and high resolution in momentum and/or angle for at least one of the reaction products.

The Hall A spectrometers have been designed for detailed investigations of the structure of nuclei, often utilizing the $(e, e'p)$ reaction. The measurements extend the range of momentum transfer and internal nucleon momenta

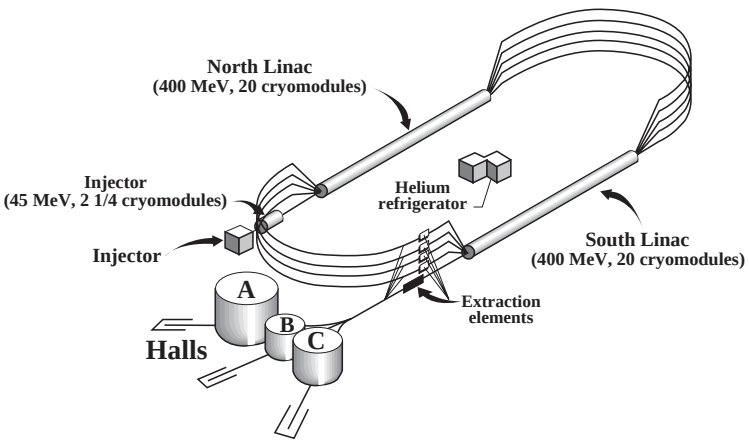

Fig. 1. Layout of the CEBAF facility. The electron beam is produced at the injector by illuminating a photocathode and then accelerated to 45 MeV. The beam is then further accelerated in each of two superconducting linacs, through which it can be recirculated up to four times. The beam can be extracted simultaneously to each of the three experimental halls.

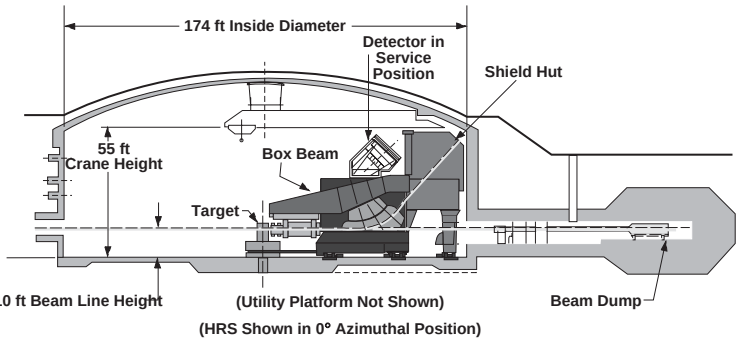

Fig. 2. Schematic cross section of Hall A with one of the HRS spectrometers in the (fictitious) 0° position.

investigated well beyond the previously known region. Such measurements could reveal the limitations of the conventional picture of nuclear structure, based on nucleons interacting via meson exchange, which is adequate for describing the low momentum-transfer regime. Experiments of this type in heavy nuclei expand our understanding of nuclear structure, and provide information on how the nucleon's properties change when it is embedded in the nuclear medium. In few-body systems, where exact calculations can be performed for interacting nucleons, these experiments may reveal the complete breakdown of the meson-exchange picture. More realistically, one hopes to establish that quark models will simply offer a much more economical description of the experimental data. The spectrometers must have high resolution to be able to isolate the different reaction channels in nuclei so that a clean comparison with theory can be achieved. High absolute accuracy is required to separate the various types of electromagnetic currents contributing to the interaction.

Studies of the electromagnetic and weak neutral current structure of the nucleon are also a major part of the Hall A program. The HRS devices have been used to measure the charge [3] and magnetic [4] form factors of nucleons with high precision. Virtual [5] and real [6] Compton scattering experiments complement these data, and a detailed study of spin observables in the $N \rightarrow \Delta$ transition [7] has been performed. An extensive program has been developed to study the spin structure of the neutron using a polarized ^{3}He target. The strange-quark contributions to the charge and magnetization distributions of the nucleons have been investigated via very precise parity-violating electron scattering experiments [8]. Together these experiments provide stringent tests of nucleon structure models.

2. High resolution spectrometers

The core of the Hall A equipment is a pair of identical 4 GeV/c spectrometers. Their basic layout is shown in Fig. 5. The vertically bending design includes a pair of superconducting cos(2θ) quadrupoles followed by a 6.6 m long dipole magnet with focussing entrance and exit polefaces and including additional focussing from a field gradient, n, in the dipole. Following the dipole is a third superconducting cos(2θ) quadrupole. The second and third quadrupoles of each spectrometer are identical in design and construction because they have similar field and size requirements. The main design characteristics of the spectrometers are shown in Table 1.

2.1. Design choices

The selection of a QQD$_n$Q magnet configuration with a vertical bend using superconducting magnets was driven by many requirements. These included: a high momentum resolution at the 10^{-4} level over the 0.8 to 4.0 GeV/c momentum range, a large acceptance in both angle and momentum, good position and angular resolution in the

Table 1
Main design characteristics of the Hall A high resolution spectrometers; the resolution values are for the FWHM

Configuration	QQD_nQ vertical bend
Bending angle	45°
Optical length	23.4 m
Momentum range	0.3–4.0 GeV/c
Momentum acceptance	$-4.5\% < \delta p/p < +4.5\%$
Momentum resolution	1×10^{-4}
Dispersion at the focus (D)	12.4 m
Radial linear magnification (M)	−2.5
D/M	5.0
Angular range	
HRS-L	12.5–150°
HRS-R	12.5–130°
Angular acceptance	
Horizontal	±30 mrad
Vertical	±60 mrad
Angular resolution	
Horizontal	0.5 mrad
Vertical	1.0 mrad
Solid angle at $\delta p/p = 0$, $y_0 = 0$	6 msr
Transverse length acceptance	±5 cm
Transverse position resolution	1 mm

scattering plane, an extended target acceptance, and a large angular range. The ultimate design choice struck a balance between capital expenditure and operating costs through many compromises between the various requirements. Here the most salient arguments are summarized.

(1) The vertical bend decouples to first order the measurement of the event's vertex position along the target from the scattered particle's momentum. When used with an extended target, a horizontal bend would have required a detector in front of the spectrometer in order to separate extended-target from momentum effects. This would have potentially limited the luminosity and compromised the momentum and angle resolution due to multiple scattering.

(2) A quadrupole after the dipole makes it possible to have a reasonably good horizontal position and angular resolution. Here one must try to minimize the first-order transverse matrix elements $\langle y|y_{tg}\rangle$ and $\langle y|\phi_{tg}\rangle$. In all designs explored with no quadrupole after the dipole, forcing either term to be appropriately small caused the other to become too large.

(3) The 45° bend is a compromise between cost and performance. A larger bend angle would produce a better momentum resolution capability and a more favorable focal plane angle, ensuring a better momentum resolution at the extremes of the momentum acceptance. However, with a 4 GeV/c central momentum the cost of a bending magnet, particularly in a spectrometer with a relatively large vertical acceptance, grows rapidly with bend angle. A more quantitative explanation of the choice of 45° appears later.

(4) The use of an indexed dipole simplified the spectrometer design considerably. Midway into the design process a QQQDQQ design was considered in order to achieve the desired momentum, position, and angular resolution with a minimum bend angle. This design included a very simple uniform-field dipole or a pair of uniform-field dipoles. Two of the quadrupoles were needed in front of the dipole to achieve the desired angular acceptance and produce a parallel beam in the radial plane, thereby maximizing the amount of resolving power achieved for the bend angle. A third quadrupole was needed in front of the dipole to accommodate extended targets. The first quadrupole after the dipole focused the parallel beam. The second was needed to achieve the desired position and angular resolution as described above. Introducing an indexed dipole [9] eliminated the quadrupoles immediately before and after the dipole as well as moderating the design parameters for the remaining quadrupoles. The design field gradient in the larger quadrupoles went from 5 to 3.5 T/m. The focussing achieved by those two quadrupoles was absorbed into the dipole. Overall the effect was to increase the cost and complexity of the dipole but greatly reduce the cost of the quadrupoles and reduce the overall length as well. The radial beam envelope is slightly divergent going into the dipole and slightly convergent coming out. This causes an insignificant reduction in the resolving power compared to a parallel option. The choice of an indexed dipole did lead to more stringent alignment tolerances than those of a homogeneous dipole.

(5) Because the design called for high quality fields in large-aperture high field-gradient magnets, superconducting $\cos(2\theta)$ quadrupoles were chosen. Normal conducting magnets would have been enormous and would have greatly limited the

angular range. Hybrid magnets like those used for the High Momentum Spectrometer (HMS) in Hall C were considered but rejected on the basis of field quality. Arguments in favor of the cos(2θ) design included the ability to incorporate higher-order multipole windings (sextupole and octupole) in the design which would minimize second- and third-order optical aberrations. These windings were included in the magnet design, but due to an undetected manufacturing error the sextupoles were installed rotated 90° from the correct orientation, rendering them useless. Correcting the error after manufacturing would have been extremely costly and time consuming. As a result, these windings were therefore never used. The aberrations were corrected for in the tracking analysis with minimal impact on the final resolution. One consequence of not using the sextupole winding in the third quadrupole, Q3, is that the "focal plane", which by design should have been at an angle of 45° to the central trajectory, is rotated to 70°. All references in this work to the detector focal plane refer to the first plane of the Vertical Drift Chambers (VDC).

(6) Both superconducting and normal conducting options were considered. Normal conducting had the advantage of being a well-established technology that was very likely to produce a robust, inexpensive magnet with almost no risk of failure. However, an evaluation of the operating costs for such a large dipole showed the superconducting option to be more favorable.

2.2. Optics design

In the standard TRANSPORT formalism [10] (see Fig. 3) the trajectory of a charged particle through a system of magnetic elements is represented by a vector (single-column matrix)

$$\vec{x} = \begin{bmatrix} x \\ \theta \\ y \\ \phi \\ l \\ \delta \end{bmatrix} \quad (1)$$

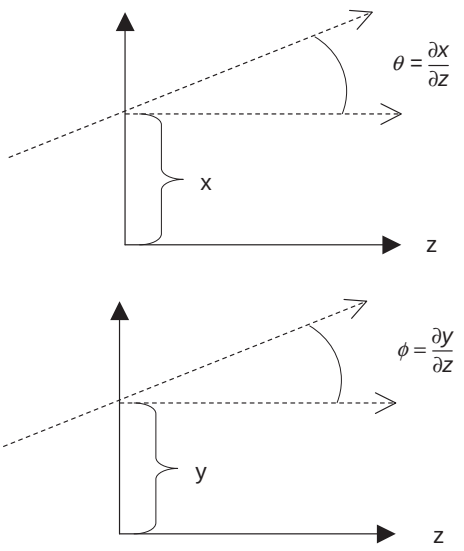

Fig. 3. Coordinates in the TRANSPORT convention. z is defined by the central or reference trajectory. x and y are perpendicular to z, with x in the dispersive plane.

where x is the displacement, in the dispersive plane, of the trajectory relative to the reference trajectory (for HRS x is in the vertical direction), θ is the tangent of the angle this trajectory makes in the dispersive plane with respect to the reference trajectory ($\theta = \mathrm{d}x/\mathrm{d}z$, where z is the direction of the reference trajectory), y and ϕ are equivalent to x and θ in the transverse plane (for the HRS y is in the horizontal direction), l is the path length difference between the trajectory and the reference trajectory, and δ ($\Delta p/p$) is the fractional deviation of the momentum of the trajectory from the central trajectory. The orientation of the x, y, and z-axes are such that $\hat{z} = \hat{x} \times \hat{y}$. To first order, the transfer of a charged particle from the interaction point ($\vec{x}_{\mathrm{tg}}$) through a series of magnets to the focal plane ($\vec{x}_{\mathrm{fp}}$) can be represented by a simple matrix equation.

The z-dependence of the spectrometer's first-order transfer matrix elements is shown in Fig. 4. The front quadrupole, Q1, is convergent in the radial (vertical) plane. Transverse focussing is provided in a nearly symmetrical way by the quadrupoles Q2 and Q3. The optics design resulted in a shallow minimum of $\langle y|\phi_{\mathrm{tg}}\rangle$ inside the dipole, which ensured a maximum horizontal

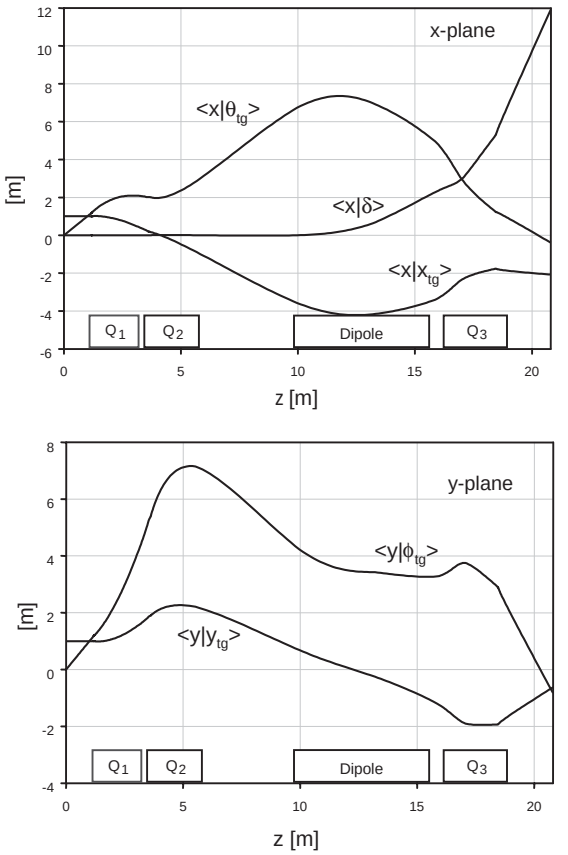

Fig. 4. First-order trajectories in a High Resolution Spectrometer. The bottom (top) graph shows the evolution of the first-order matrix elements in the horizontal (vertical) plane, as a function of the trajectory length. The location of the four magnetic elements is also indicated.

angular acceptance at a given dipole gap size. The $\langle y|y_{\rm tg}\rangle$ term remains small ($\leqslant 2.5$) all the way through the spectrometer, allowing the use of extended targets (10 cm at 90°) with no substantial loss in solid angle.

In the radial plane, the $\langle x|\theta_{\rm tg}\rangle$ term is kept large inside the dipole to make efficient use of the dipole width to build resolving power in spite of the modest bending angle. Radial focussing is given by the 30° tilt angle at the entrance and exit pole faces and by the introduction of a negative first-order field index, $n = -1.25$.

The design first-order transport matrix in "natural units" (meters, dimensionless, and fractional δ's) at the focus is

$$\begin{bmatrix} x_{\rm fp} \\ \theta_{\rm fp} \\ y_{\rm fp} \\ \phi_{\rm fp} \\ \delta_{\rm fp} \end{bmatrix} = \begin{bmatrix} -2.48 & 0.0 & 0.0 & 0.0 & 12.4 \\ -0.15 & -0.40 & 0.0 & 0.0 & 2.04 \\ 0.0 & 0.0 & -0.40 & -1.30 & 0.0 \\ 0.0 & 0.0 & 0.54 & -0.78 & 0.0 \\ 0.0 & 0.0 & 0.0 & 0.0 & 1.0 \end{bmatrix} \times \begin{bmatrix} x_{\rm tg} \\ \theta_{\rm tg} \\ y_{\rm tg} \\ \phi_{\rm tg} \\ \delta \end{bmatrix}. \quad (2)$$

Notice that the transverse matrix is neither point to point, $\langle y|\phi_{\rm tg}\rangle = 0$, nor parallel to point, $\langle y|y_{\rm tg}\rangle = 0$. This compromise was driven by the need for a simultaneous good resolution in the transverse position, $y_{\rm tg}$, and angle, $\phi_{\rm tg}$.

Practical considerations led to certain constraints on the optical design, some of which are listed below:

- The beam envelope was constrained not to exceed 0.25 m (0.8 m) in the dipole gap (width), and 0.3 m (0.6 m) diameter in the useful aperture of Q1 (Q2, Q3). These size constraints helped limit the cost of the magnets.
- The bend angle was kept at 45°. This value was selected at an early stage of the design as a reasonable compromise for a high-energy, high-resolution spectrometer, under the assumption that the detector system would provide a spatial resolution of 100 μm. The following expression is based on first-order optics principles [11]:

$$\frac{D_x}{M_x}\Delta\theta = -2\omega\tan\frac{\alpha}{2} \quad (3)$$

relates the resolving power ($\propto D/M$ with D being the dispersion and M the magnification) and angular acceptance in the radial plane ($\Delta\theta$) to the bend angle (α) and the dipole half-width

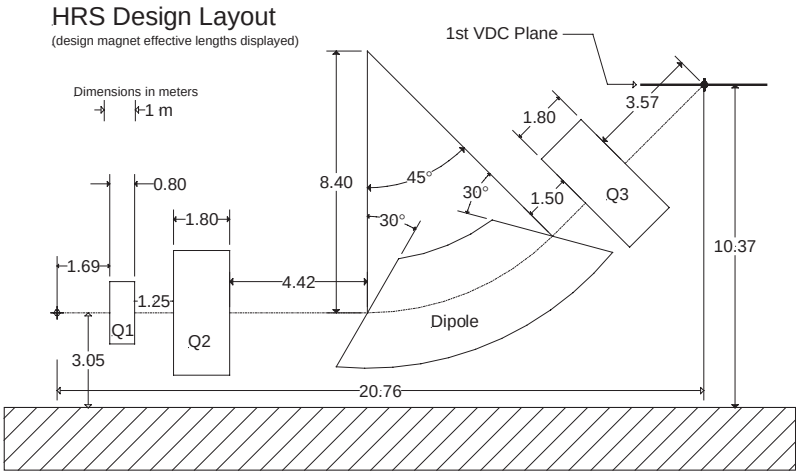

Fig. 5. Schematic layout of a HRS device, showing the geometrical configuration of the three quadrupole and the dipole magnets. Also shown is the location of the first VDC tracking detector.

(ω). For $\Delta\theta = \pm 60$ mrad, $\omega = 40$ cm, and $D/M = -5$, the above expression gives $\alpha = 41^\circ$, close to the chosen value of 45°. The expression assumes a parallel beam in a uniform-field dipole. The radial focussing provided by the indexed dipole necessitates a slightly larger bend angle.

- The pole-face rotation angles have been fixed at -30° as a practical limit. The field of Q1 and the dipole field index provide the remaining radial focussing. In the absence of the field index an excessively large rotation angle ($\sim 43^\circ$) would have been needed.
- The overall optical length was constrained to fit with 24 m.

2.3. Spectrometer Mechanical Support System

A schematic view of one of the Hall A High Resolution Spectrometers (HRS) is shown in Fig. 5. The structural system of each spectrometer arm must rigidly support the spectrometer magnet and detector elements in their 45° vertical bending configuration, while providing almost full azimuthal positioning of the spectrometer about the central pivot. All three quadrupoles and the drift chamber detector elements are hung from or mounted on a box beam, which is rigidly mounted on the top of the dipole. Once these elements are surveyed in place, their relative positions remain constant regardless of the spectrometer azimuthal position. The box beam itself is an ~ 80 Mg welded steel structure. The back of the box beam extends into the shield house. The detector package and the box beam holding it are surrounded by the shield house, but free to move within it (see Fig. 2).

The 450 Mg concrete shield hut required for the detectors is independently supported and positioned from a structural steel gantry. The bulk of its mass is transmitted from the structural leg to a 20.7 m radius steel floor track through a series of bogie-mounted conical wheels (see Section 2.8). The rest of its weight is supported on the back end of the transporter cradle. The total mass of each spectrometer including the shielding hut is over 1000 Mg.

2.4. Cryogenics and magnet cooling system

The two spectrometers contain a total of eight superconducting magnets, two dipoles and 6 quadrupoles. These magnets each have independent cryogenic controls and reservoirs. The cryogenic system that maintains these magnet systems is common to all eight magnets and the cryo-target. The cryogenic system is fed from an 1800 W helium refrigerator, the End Station Refrigerator (ESR), dedicated to the cooling of the magnets and targets in all JLab end stations.

2.4.1. Cryogenic Distribution System

Hall A has a Cryogenic Distribution System (CDS) that supplies helium and liquid nitrogen (LN_2) cryogens from the ESR to the eight superconducting magnets. The CDS also supplies helium cooling to the cryotarget which can operate at either 15 K or 5 K depending on the choice of target. The CDS consists of fixed rigid transfer lines, two flexible links that permit rotation of the spectrometers, an internal cool-down heat exchanger, and flexible U-tubes to connect individual magnets to the system. The cool-down heat exchanger uses LN_2 and a gas blending circuit to pre-cool 10 g/s helium gas at 0.4 MPa to any temperature from 250 to 80 K. This variable temperature source is used to perform a programmed cool down and warm up of the magnets. Under normal operation the CDS supplies supercritical helium gas at 0.24 MPa and 4.5 K to each magnet where it is expanded through a local Joule-Thompson (JT) valve to produce liquid helium. The cold gas from the JT expansion and the magnet boil off is returned through the CDS cold return. LN_2 is supplied at 0.4 MPa and 80 K to each magnet where the nitrogen is expanded through a local JT valve to produce liquid nitrogen. The nitrogen gas from JT expansion and boil off is vented to the atmosphere through an exhaust line. Warm helium is collected and returned to the ESR through a purifier. Further discussion of the Hall A CDS can be found in Ref. [12].

2.4.2. Typical magnet cryogenics controls system

Each of the eight magnets has a set of cryogenic control valves, liquid level devices, temperature sensors and pressure sensors. The magnets each have individual LN_2 and He reservoirs. These devices are monitored by an Experimental Physics and Industrial Control System (EPICS)[6] control system that monitors the sensors, logs system data, generates interlocks, and has proportion, integral, derivative (PID) loops for valve control. Each magnet has helium top fill, bottom fill and cold return valves, and LN_2 top and bottom fill valves. Warm valves also control current cooling and warm gas return for cool down. Normal steady-state operation consists of maintaining the liquid level in the helium and LN_2 reservoirs using a PID control of the helium top fill valve. Current lead cooling is maintained by MKS mass flow controllers. Typical interlocks are liquid level low, current-lead mass flow low, magnet temperature high, and vacuum high. Data and history are available on-line through custom user-defined strip charts.

2.5. Magnet power supplies

The first quadrupole (Q1) of each spectrometer is powered by a Danfysik[7] System 8000, model 853 power supply specified to deliver 3500 A at 5 V with a stability of 50 ppm of the full current over 8 h. The second and third quadrupoles (Q2 and Q3 respectively) are each powered by an FuG[8] model NTN 20000SUM-10 power supply specified to deliver 2000 A at 10 V with a stability of ± 10 ppm (full current, 8 h). Operationally, over an 8 h period, their stability has been found to be a factor of 2–3 worse than the specification and the short-term stability (10–20 min) even worse (± 400 ppm). Each of the dipoles is powered by a Dynapower Corporation[9] model PD42-01000202-FKLX-3569 power supply specified to deliver 2000 A at 10 V with an stability of ± 10 ppm (10–100% of full current, 8 h). Several years of operation have established that these supplies are actually stable to ~ 3–4 ppm.

The protection systems used by the various Hall A magnets are similar in both method and basic implementation. For all Hall A magnets the electrical circuit consists of three elements connected in parallel across the power supply output terminals. In order of increasing distance from the power supply, we find (a) a reverse-biased bank of power diodes with a forward-biased resistance of several milliohms, (b) a dump resistor and, (c) the magnet coil. The dump resistor values are 0.063 Ω

[6] EPICS documentation, www.aps.anl.gov/epics.

[7] Danfysik A/S, Mollehaven 31, DK-4040 Jyllinge, Denmark, www.danfysik.dk.

[8] F. u. G. Elektronik GmbH, Florianstrasse 2, D-83024 Rosenheim, Germany, www.fug-elektronik.de.

[9] Dynapower Corporation, P.O. Box 9210, South Burlington, VT 05407, USA, www.dynapower.com.

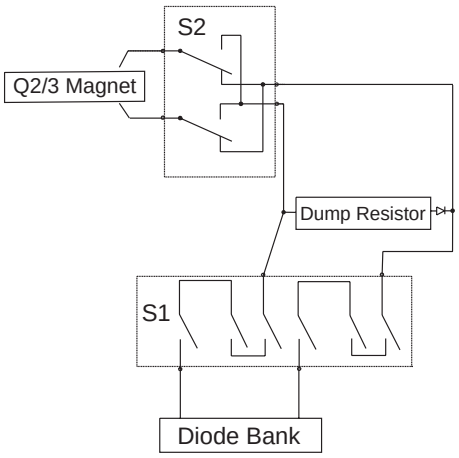

Fig. 6. Dump resistor and power supply switching scheme for the Q2 (and Q3) quadrupole magnet.

for Q1 and 0.125 Ω for the other magnets. In the case of Q2, Q3 and the dipole, zero-flux current transformers measure directly the current flowing through the magnet coil. For Q1 the current measured by the power supply flows through both the magnet and the dump resistor.

Where the various magnet systems differ is in the location of the switches and in their operation. For the case of Q2 and Q3, a double-pole, single-throw (DPST) switch (S1) is located between the diode bank and the dump resistor (see Fig. 6). When it opens, it separates the FuG diode bank combination from the remaining circuit. A double-pole, double-throw (DPDT) switch (S2) located between the dump resistor and the quadrupole coil allows a quick reversal of the quadrupole polarity. During normal operation, the FuG output power stage will be engaged (on) and S1 will be closed. In case of an emergency, the energy stored in Q2 or Q3 can be dissipated in two ways. A "slow dump" consists of just turning off the FuG power stage. This forward-biases the diode bank allowing the quadrupole current to flow through the diodes with a small fraction flowing through the dump resistor. In this case, the energy stored in a fully excited quadrupole ($\sim$0.6 MJ) is dissipated in a couple of minutes. A "fast dump" turns the FuG power stage off and also opens switch S1. This forces the quadrupole current to flow through the dump resistor, discharging a fully excited quadrupole in about 4 s. The Q1 power circuit is similar to the one for Q2 and Q3 except that both S1 and S2 are located between the diode bank and the dump resistor. A fast dump dissipates the maximum energy stored in Q1 ($\sim$0.13 MJ) in about 1.5 s.

In the case of the Dynapower supplies, a single-pole, single-throw (SPST) switch (M3) is located between the supply power output stage and the diode bank. Also, the diode bank has a SPST switch (M4) in series with it. There is no switch to reverse the dipole polarity. This operation has to be performed manually. During normal dipole operation, the Dynapower power stage will be engaged (on), and both M3 and M4 will be closed. A "slow dump" fault turns the Dynapower power stage off and opens M3. As in the case of the quadrupoles, the diode bank gets forward-biased, discharging a fully excited dipole ($\sim$5 MJ) in about 20 min. A "fast dump" turns the power stage off and opens both M3 and M4 forcing the dipole current to flow through the dump resistor. A fully excited dipole will discharge in about 30 s.

All critical magnet protection systems are implemented in hardware with no software involved. Electronic circuits monitor the voltage across the normal-to-superconducting wire transitions (leads) as well as the voltage difference between the two half-lengths of superconducting wire used in the magnet construction. In the case of the dipole the half-length corresponds to one of the coils while in the case of Q2 and Q3 it corresponds to two of the four quadrants. The voltage taps are located so that no piece of superconducting wire goes unmeasured. If any of these voltages exceeds a set threshold, a fast dump of the magnet is initiated. A slow dump is initiated if the helium level or the rate of helium flow through the leads drops below a set threshold. If the helium flow rate through the leads drops to exceedingly low values, a fast dump is initiated. A passive interlock chain is used to determine that all the wiring and circuitry involved in the protection of the magnet is connected and powered. A failure of this interlock will initiate a slow dump.

The protection system used for the right spectrometer dipole, for reasons discussed in the next section differs from that described above.

Lead voltages above threshold or exceedingly low helium flow rate through the leads will trigger a fast dump as discussed above. One difference is that low helium levels or lead flow rates trigger a controlled ramp down of the dipole current by the power supply instead of a slow dump. Another difference is that a voltage asymmetry between the two coils above threshold triggers a slow dump and not a fast dump.

The Q1 protection circuit is also different. Instead of comparing the voltage across the two halves of the coil as in the case of the other magnets, the protection system measures the voltage across the entire coil and across one of the quadrants. This method eliminates the possibility that a quench occurring at half the length of the superconducting cable propagates symmetrically in both directions of the cable so that, although a quench has occurred, the voltage difference between the two halves of the cable remains zero. The conditions required to trigger a Q1 slow or fast dump are similar to those for the Q2, Q3 quadrupoles except that the lead temperature is also monitored. If it is found above a threshold value, a fast dump is initiated.

The EPICS control system described in Section 6 is used to remotely operate the various magnet power supplies as well as monitor all the magnet signals including those used for protection (via isolation amplifiers).

2.6. Magnet commissioning and field mapping

The process of commissioning the magnets for the left (w.r.t. the beam direction) spectrometer (HRS-L) dipole was uneventful. Tests were performed on the various power supplies and cryogenic systems to verify that all systems worked according to specifications and all interlocks functioned as expected. Early in the testing of the HRS-R dipole, on the other hand, a catastrophic event occurred after which the magnet behaved differently from the left dipole (HRS-L). Asymmetric voltages in the two halves of the coil, an excessive helium boil-off at normal current ramping rates, and a sluggish response of the measured magnetic field compared to the current in the magnet were among the most significant observables. It is believed that one half of the superconducting coil developed a normal conducting short. Rather than invest a considerable amount of time and money disassembling the magnet, which was already built into the spectrometer superstructure, it was decided to use the magnet as is with administrative limits on its operation. Those limits are: the current may not exceed 1145 A and the ramping rate must be kept less than 0.15 A/s. Operationally, this translates into a maximum central momentum of about 3.16 GeV/c with slower field changes. Ramping from zero to full current takes more than 2 h plus an additional thirty minutes for the magnetic field to stabilize.

A detailed description of the magnetic field mapping can be found in Ref. [13]. Accuracies at the 10^{-3} level were achieved in the mapping. Quadrupoles were mapped using axially segmented rotating coils, providing a measurement of the effective length to within 5×10^{-4}. The dipoles were mapped using Hall probes mounted on a non-magnetic carriage drawn through the magnet on rails connected to the magnet poles. As a result the effective magnetic length of the dipoles is known to within ± 5 mm.

2.7. Field monitoring

Magnetic fields in each dipole are measured and monitored using two arrays of three NMR field probes, providing a field range from 0.17 to 2.10 T. The arrays are mounted in an aluminum fixture placed at the vertical edges of the trajectory envelope about 1.5 m inside the magnet entrance. The probes are equipped with field-gradient compensating coils to locally eliminate the field gradient in the magnet. The probes are connected through a multiplexer to a PT 4025 Teslameter.[10] This system is very accurate, giving field readings at the 10^{-5} level. Supplemental to the NMR probes, each magnet has a Hall probe mounted in the vicinity of the NMR probes. The Hall probes are read out with Model 450 Gaussmeters.[11] In

[10] Metrolab Instruments SA, 110 Ch. du Pont du Centenaire, CH-1228 Plan-les-Ouates, Geneva, Switzerland.

[11] Lake Shore Cryotronics Inc., 575 McCorkle Blvd., Westerville, OH 43082-8888, USA.

general, the Hall probes are used only as a backup for the NMR probes. The Hall probes are used also in low field (low momentum) operation.

The quadrupole fields are monitored using Hall probes and Model 450 Gaussmeters. Because the Hall probes cannot be relied upon for long-term stability and reproducibility, fields are set in the quadrupoles based on their current settings. The current is measured using a zero-flux current transformer readout with an HP 3458 Precision DVM.[12] While the quadrupole magnets are current-dominated, there is some hysteresis effect in the field due to the iron collar. This effect was measured to be large enough in Q2 and Q3 to warrant cycling of those magnets. As a consequence care is taken to cycle the quadrupoles before setting them to the desired current value. This is done by always going to the nominal maximum current of 1600 A before going to the desired current. The hysteresis effect in Q1 is small enough that cycling is not required. No cycling is required in the dipoles, because no cycle dependence was observed in the field profile during field mapping.

2.8. Positioning and alignment

At the floor level, each HRS is composed of three sections: a central carriage (the cradle, a 16 Mg steel structure), a detector shield house gantry and a link. The cradle moves on two trains of wheels. The front train (towards the target) is composed of two four-wheeled carriages called bogies. The back train is composed of two eight-wheeled bogies. The cradle holds the spectrometer proper via three vertical-stroke hydraulic jacks, which allow adjustment of the spectrometer height, roll and pitch at each azimuthal position. One jack is located at the front of the dipole while the other two are at the back. At present, a manual procedure is used to adjust the jacks in order to correct gross misalignments. A pair of horizontally mounted hydraulic jacks at the back of the dipole can be used to rotate by up to $\pm 0.5^\circ$ the whole spectrometer around the hydraulic jack supporting the front of the dipole. These jacks are also operated manually and can be used to correct gross horizontal mispointing of the spectrometer. The detector shield house front legs rest on the back of the cradle while the back legs move on four bogies. A platform extending between the back of the cradle and the back legs of the gantry carries the magnet power supplies and protection electronics, field- and current-measuring devices and the spectrometer motion control systems and related servo-amplifiers. A link attached between the cradle and the central bearing constrains the radial motion (i.e. towards or away from the target) of the cradle and detector shield house gantry while allowing them to rotate around the central bearing.

The transporter cradle rides along two concentric steel floor plates (with radii of 9.36 and 16.55 m) through a series of eight-wheeled bogies. Each bogie is rated for 230 Mg. Each 610 mm diameter conical wheel is rated for 596 kN when mounted on a 832 N/m Bethlehem rail.[13] Azimuthal drive is accomplished by a pair of electronically synchronized servo-drive gear reducers, each of which powers a pair of bogie wheels. One pair of drive wheels is at the inner radius location; the other is at the outer. By this means the drive traction can be balanced about the spectrometer pivot, thus minimizing transporter twist and reaction force at the central bearing. Azimuthal pointing is maintained by a central bearing which is pin connected to the transporter cradle through a massive link which allows elevation and pitch motion, but only minimal ''yaw'' (pointing error). One wheel of each bogie is driven by a servomotor through a gear reducer. A VME system based on the real-time operating system VxWorks[14] and a custom-made Tcl/Tk interface [72] are used to monitor and control the motion of each spectrometer. The maximum speed is 3° per minute.

The roll and the pitch of each of the spectrometers are measured by a bi-axial inclinometer[15]

[12] Hewlett Packard, Palo Alto, CA, USA, www.hp.com.

[13] Whiting Corporation, 26000 Whiting Way, Monee, IL 60449, USA.

[14] Wind River, Alameda, CA, USA, www.wrs.com.

[15] Applied Geomechanics Incorporated, 1336 Brommer Street, Santa Cruz, CA 95062, USA, model 711-2.

located at the back of the dipole. Each inclinometer axis has a range of ± 7.5 mrad and a resolution of 1 μrad. Calibration data provided by the factory for each of the inclinometers over their full tilt range and at several temperatures is used to correct the raw readings for non-linearity and temperature effects.

The angular position of the spectrometers with respect to the beam line is determined from marks etched into the floor at a nominal distance of 10 m from the hall center. To layout the marks, a template with several slots was built, each slot corresponding to a floor mark. The location of the slots to reference points in the template was measured. The template was then laid out in the hall and its location measured and adjusted until the separation of the slots was equivalent to $0.5^\circ \pm 0.0006^\circ$. A support arm attached to the bottom front end of the dipole holds a ruler that slides over the floor marks. A closed circuit television camera mounted on a linear translation stage is used to read the location of the floor marks on the ruler to avoid uncertainties from parallax. The position of the floormarks can be established to within 1 mm. The raw angular readings are then corrected for spectrometer roll/pitch and offset in the location of the support arm w.r.t. the spectrometer central ray.

By design, the spectrometers are not constrained to remain along a radius as they move around the hall central bearing. Various factors like the arc-length, direction and speed of the move change the spectrometers pointing by as much as ± 4 mm in a non-reproducible manner. An automated measurement of such spectrometer mispointing was found to be more troublesome than anticipated during the spectrometer design phase. The large number of lines (cryogenic, power, water and signal), routed through the pivot area, and the target system prove to be significant obstacles for such a design. The chosen method would also have to be radiation resistant if implemented near the pivot area. An interim solution for those experiments which use the standard Hall A scattering chamber has been to use a linear variable differential transformer (LVDT) to measure the gap between an arm parallel to the spectrometer mid-plane and the outer surface of the scattering chamber. Raw values are corrected for LVDT non-linearity, chamber location and eccentricity as well as spectrometer roll. Operational experience with the system has uncovered two major problems: (a) it is easily disturbed any time that maintenance or repair work is performed around the pivot area, and (b) the LVDT read-out controllers, being microprocessor based and located on the power supply platform, are prone to have their internal calibration constants affected by radiation. Because of these problems, the system requires a great deal of attention and the results can vary widely. Nonetheless, values obtained from the LVDT/floor mark combination and from spectrometer surveys agree to within ± 0.14 mrad in spectrometer scattering angle and ± 0.4 mm in pointing over timespans of several months. The absolute uncertainty in the scattering angle is limited by the reconstruction of the scattering vertex position (see Section 9.3) rather than by the spectrometer alignment.

2.9. Collimators

Each spectrometer is equipped with a set of collimators, positioned 1.109 ± 0.005 and 1.101 ± 0.005 m from the target on the left and right spectrometers, respectively. There is a large collimator, made of 80 mm thick tungsten, with a 121.8 mm vertical opening and a 62.9 mm horizontal opening at the entrance face. The opening in this collimator expands to 129.7 by 66.8 mm at the exit face. A second smaller collimator, made of the same material, is 50.0×21.3 mm at the entrance face and 53.2×22.6 mm at the exit face. The third collimator is the sieve slit, which is used to study the optical properties of the spectrometers. The sieve is a 5 mm thick stainless steel sheet with a pattern of 49 holes (7×7), spaced 25 mm apart vertically and 12.5 mm apart horizontally. Two of the holes, one in the center and one displaced two rows vertically and one horizontally, are 4 mm in diameter. The rest of the holes are 2 mm in diameter (see Fig. 7). The sieve slits are positioned 75 mm further from the target than the other collimators. Each collimator can be selected remotely via a vertical actuator.

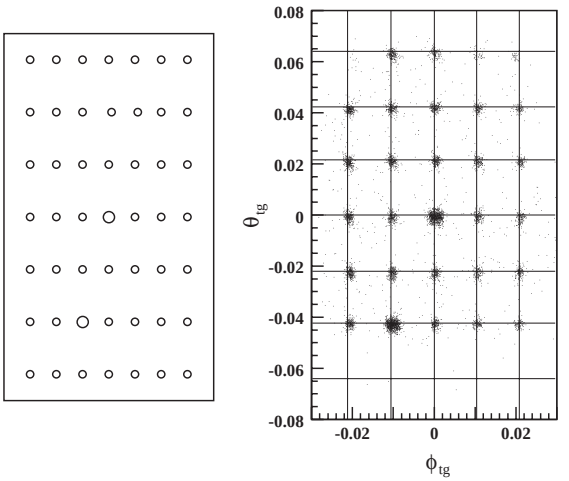

Fig. 7. Geometric (left) and reconstructed (right) configurations of the sieve slit. The large holes, which allow for an unambiguous identification of the orientation of the image at the focal plane, can be clearly identified in the right figure.

3. The detector package

3.1. General features and purpose

The detector packages of the two spectrometers are designed to perform various functions in the characterization of charged particles passing through the spectrometer. These include: providing a trigger to activate the data-acquisition electronics, collecting tracking information (position and direction), precise timing for time-of-flight measurements and coincidence determination, and identification of the scattered particles. The timing information is provided from scintillators, as well as the main trigger. The particle identification is obtained from a variety of Cherenkov type detectors (aerogel and gas) and lead-glass shower counters. A pair of VDCs provides tracking information. The main part of the detector package in the two spectrometers (trigger scintillators and VDCs) is identical; the arrangement of particle-identification detectors differs slightly. The HRS-L can be equipped with a focal-plane polarimeter to determine the polarization of detected protons. The optics of the HRS spectrometers, described in the previous section, results in a narrow distribution of particle trajectories in the transverse direction, leading to an aspect ratio of the beam envelope of about 20:1 at the beginning of the detector package and 4:1 at the end.

The detector package and all Data-Acquisition (DAQ) electronics are located inside a Shield Hut (SH) to protect the detector against radiation background. The SH is also equipped with air conditioning and fire suppression systems. The individual detectors are installed on a retractable frame, so that they can be moved out of the SH for repair or reconfiguration. The DAQ electronics are mounted on the same frame. Fig. 8 shows sideviews of the detector setups for the two HRSs, including the movable frame, the detector stack and the DAQ electronics.

3.2. Detector shielding

The shielding of the detector package consists of two parts: the Line-of-Sight Block and the SH. The Line-of-Sight Block is a two-meter thick concrete block located 2 m from the target on top of Q1 and Q2. It moderates the pion flux produced at the target and therefore leads to a reduction of the muon rate in the detectors [14]. The SH protects the detectors against radiation from all directions. It is made of a 10 cm thick steel frame with a 5 cm lead layer inside and a layer of concrete outside. The thickness of the concrete layer varies. There is neither concrete nor lead on the top of the SH, which is 1–2 m from the Hall ceiling. The concrete is 40 cm thick on the large-angle side of the SH, 80 cm on the beam-line side and 100 cm on the target side. The SH configuration was optimized using the GEANT [15] code, with the neutron yield measured by Bathow et al. [16] and meson yields measured by Boyarski et al. [17] as input. With this shielding configuration a neutron attenuation factor of 10 was obtained. The radiation level inside the SH is below 1 mrem per hour at a luminosity of 10^{38} cm^{-2} s^{-1}. At that luminosity the rate of a single spectrometer trigger can be a few hundred kHz, depending on the spectrometer momentum and angle setting.

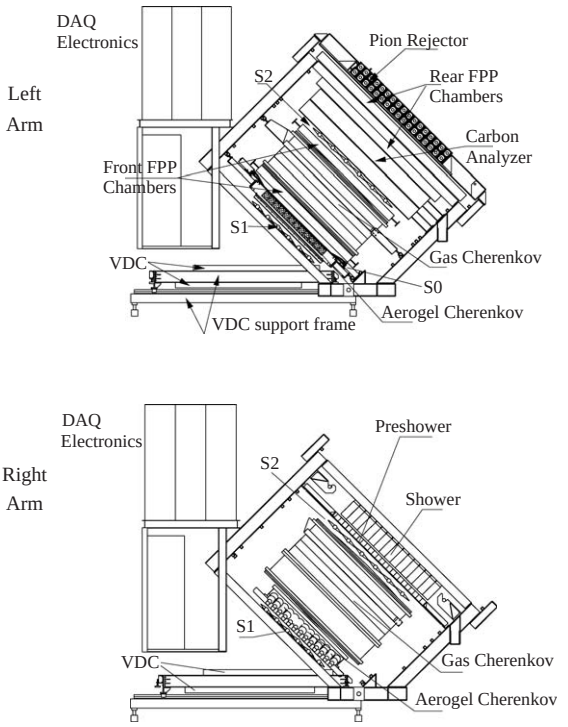

Fig. 8. Sideview of detector stack, shown in the top (bottom) figure for the left (right) (w.r.t. the beam line) HRS device. Individual elements of the detector system are indicated in the configuration used most frequently. Also shown is the position of the data-acquisition (DAQ) electronics and of the VDC support frame.

3.3. Tracking

Tracking information is provided by a pair of VDCs in each HRS, described in detail in Ref. [18]. The concept of VDCs fits well into the scheme of a spectrometer with a small acceptance, allowing a simple analysis algorithm and high efficiency, because multiple tracks are rare. The VDCs are bolted to an aluminum frame, which slides on Thomson rails attached to the box beam. Each VDC can be removed from its SH for repair using these Thomson rails. The position of each VDC relative to the box beam can be reproduced to within 100 μm.

Each VDC chamber is composed of two wire planes, separated by about 335 mm, in a standard UV configuration—the wires of each successive plane are oriented at 90° to one another, and lie in the laboratory horizontal plane. They are inclined at an angle of 45° with respect to the dispersive and non-dispersive directions. The nominal particle trajectory crosses the wire planes at an angle of 45° (see Fig. 9). There are a total of 368 sense wires in each plane, spaced 4.24 mm apart. The signals from the sense wires are shaped at LeCroy[16] amplifier-discriminator cards 2735DC mounted 30 cm away from the chamber. The logic ECL signals are then routed via 5 m long twisted-pair cables to a FastBus LeCroy TDC module 1877. The feedback of the ECL signals from these cables on the sense wires and amplifier inputs is suppressed by careful shielding of the output cables and VDCs.

The electric field of the VDCs is shaped by gold-plated Mylar planes, nominally at −4.0 kV when the standard gas mixture of argon (62%) and ethane (38%) is used. The gas is bubbled through cooled alcohol to reduce aging effects on the sense wires and flows at about 5 l per hour per chamber. The average thickness of all material encountered by particles in one chamber is 7.8×10^{-4} radiation lengths (X_0). The dominant single contributor to multiple scattering is the horizontal Ti window at the exit of the spectrometer vacuum, with a thickness of 127 μm (5×10^{-3} X_0) [19]. In the focal plane the position resolution is $\sigma_{x(y)} \sim 100$ μm, and the angular resolution $\sigma_{\theta(\phi)} \sim 0.5$ mrad. A typical wire-hit distribution and an on-line analysis of the wire efficiency are shown in Fig. 10.

During five years of operation the VDCs have run very stably, with only one broken wire, caused by over-crimping during construction.

3.4. Triggering

There are two primary trigger scintillator planes (S1 and S2), separated by a distance of about 2 m. Each plane is composed of six overlapping paddles made of thin plastic scintillator (5 mm BC408[17]) to

[16] LeCroy Corporation, Chestnut Ridge, NY 10977-6499, USA, www.lecroy.com.

[17] Bicron Newbury, 12345 Kinsman Road, Newbury, OH 44065-9577, USA.

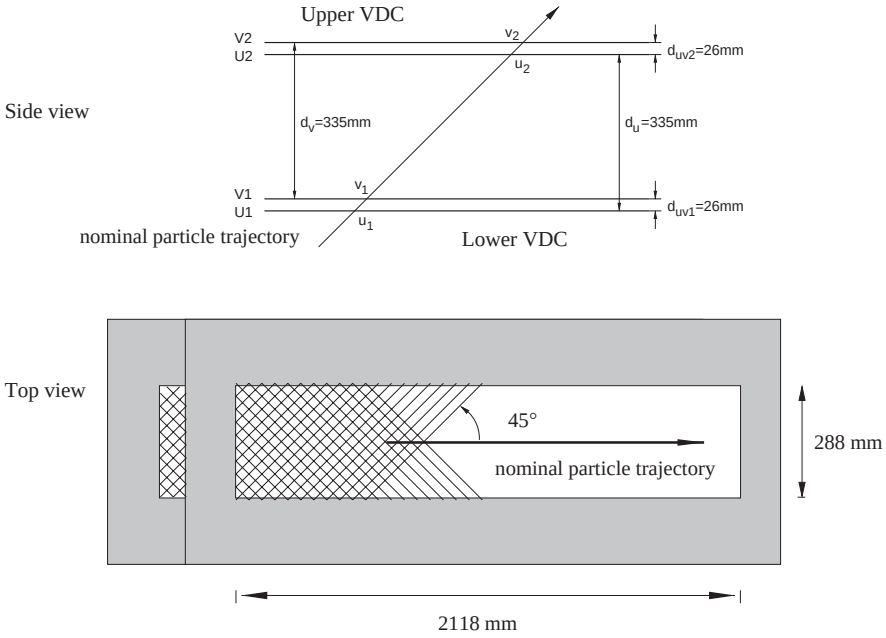

Fig. 9. Schematic lay-out of a pair of Vertical Drift Chambers for one HRS (not to scale). The active area of each wire plane is rectangular and has a size of 2118 mm × 288 mm. Each VDC consists of one U and one V wire plane. The sense wires in each of them are orthogonal to each other and lie in the laboratory horizontal plane. They are inclined at an angle of 45° with respect to both the dispersive and the non-dispersive directions. The lower VDC is as close as possible to the spectrometer focal plane. The vertical distance between like wire planes is 335 mm.

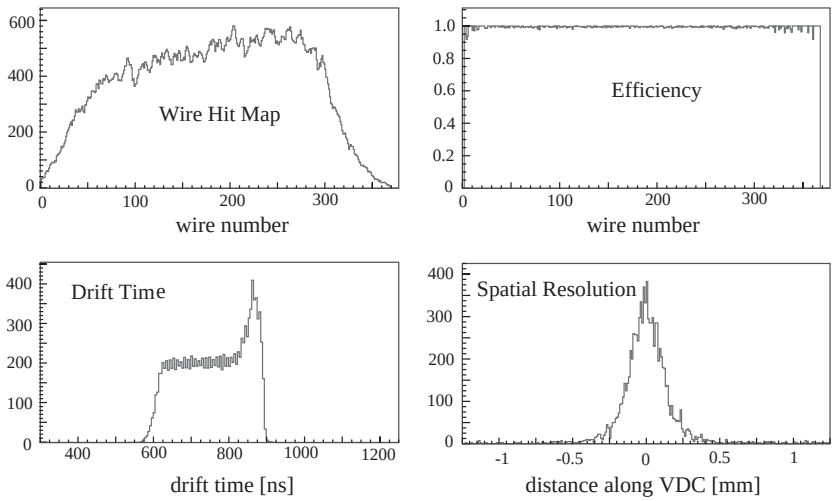

Fig. 10. Typical on-line results of the analysis of one VDC to monitor its performance: top left, response as a function of the wire number; top right, wire efficiency as a function of the wire number; bottom left, drift-time spectrum (short drift times occur at large TDC values); bottom right, spatial resolution for events with hits in six adjacent wires.

minimize hadron absorption. Each scintillator paddle is viewed by two photomultipliers (PMTs) (Burle 8575[18]). The time resolution per plane is approximately 0.30 ns (σ). For experiments which need a high hadron trigger efficiency, an additional scintillator trigger counter (S0) can be installed. The 10 mm thick S0 counter is viewed by two 3″ PMTs XP2312.[19] The information from the gas Cherenkov counter can be added into the trigger.

The trigger system is built from commercial CAMAC and NIM discriminators, delay units, logic units, and memory lookup units (MLU). A coincidence between two PMTs is made for each scintillator paddle. The logical OR of these signals is formed individually for the S1 and the S2 plane. For the gas Cherenkov detector the analog sum of the signals from its 10 PMTs is used to prepare a hit signal. The main trigger for one spectrometer is formed by the logical AND of the first and the second scintillator plane. To measure the trigger efficiency, an alternative trigger is formed by a hit in either the first or the second scintillator plane and a hit in a third detector, which can be the gas Cherenkov detector or the S0 scintillator. A coincidence trigger is made from the time overlap of the two spectrometer triggers in a logical AND unit. The various trigger signals go to the trigger supervisor module which starts the DAQ readout. Most inputs of the trigger supervisor can be individually prescaled. Triggers which are accepted by the DAQ are then retimed with the scintillators to make gates for the ADCs and TDCs. This retiming removes trigger time jitter and makes the timing independent of the trigger type.

The trigger modules are remotely programmed by CAMAC commands which are executed by a software control package. The software control reads two setup files, a map of the module locations and a list of the default CAMAC commands to set up the trigger. Alternatively, the CAMAC commands can be executed remotely using a graphical user interface (GUI) which displays the available units and their location in the trigger. The setup is sufficiently flexible to allow rapid inclusion of new trigger elements or detector systems.

To exploit the ability of the facility to measure small coincidence cross sections, experiments often run with high rates on the order of 1 MHz in a single scintillator plane. Because the dead times of the various components are typically 30 ns and larger, and the pulse width of the trigger signals was as much as 100 ns for some experiments, an electronics dead time on the order of 3–10% can be expected, and has to be monitored accurately for cross-section measurements. For this purpose, a well-defined electronic pulse is added in the analog circuitry to the scintillator pulses before the discriminator. These pulses are traced through the trigger into the data stream by forming the logical AND between the trigger and the pulser and putting this result into scalers and TDCs to see where they get lost or what time shifts occur due to pile-up. A 1 Hz pulse is sent into the four PMTs required to make a trigger, with each scintillator paddle fired in turn, thus measuring the dead time differentially across the focal plane.

3.5. Particle identification

The long path from the target to the HRS focal plane (25 m) allows accurate time-of-flight identification in coincidence experiments if the accidental rate is low. After correcting for differences in trajectory lengths, a TOF resolution of ~ 0.5 ns (σ) is obtained (see Fig. 11). The time-of-flight between the S1 and S2 planes is also used to measure the speed of particles β, with a resolution of 7% (σ) (see Fig. 11).

A gas Cherenkov detector filled with CO_2 at atmospheric pressure [20] is mounted between the trigger scintillator planes S1 and S2. The detector allows an electron identification with 99% efficiency and has a threshold for pions at 4.8 GeV/c. The detector has ten spherical mirrors with 80 cm focal length, each viewed by a PMT (Burle 8854, see footnote 18); the light-weight mirrors were developed at INFN [21]. The focusing of the Cherenkov ring onto a small area of the PMT photocathode leads to a high current density near

[18] Burle Electron Tubes, 1000 New Holland Ave., Lancaster, PA 17601-5688, USA.

[19] Photonis, Avenue Roger Roncier, Z.I. Beauregard, B.P. 520, 19106 Brive Cedex, France.

the anode. To prevent a non-linear PMT response even in the case of few photoelectrons requires a progressive HV divider [22]. The length of the particle path in the gas radiator is 130 cm for the gas Cherenkov in the HRS-R, leading to an average of about twelve photoelectrons. In the HRS-L, the gas Cherenkov detector in its standard configuration has a pathlength of 80 cm, yielding seven photoelectrons on average. The total amount of material in the particle path is about 1.4% X_0.

Two layers of shower detectors [23] are installed in each HRS. The structure of the shower detectors in each arm is shown in Fig. 12. The blocks in both layers in HRS-L and in the first layer in HRS-R are oriented perpendicular to the particle tracks. In the second layer of HRS-R, the blocks are parallel to the tracks. The front layer in HRS-R is composed of 48 lead glass blocks, 10 cm × 10 cm × 35 cm. The second layer is composed of 80 lead glass blocks, 15 cm × 15 cm × 35 cm each. The front layer in HRS-L is composed of 34 lead glass blocks, of dimensions 15 cm × 15 cm × 30(35) cm. The second layer is composed of 34 similar blocks. Because of its reduced thickness, the resolution in HRS-L is not as good as that of the shower detector in HRS-R. A particle identification parameter R_{sh} is defined as

$$R_{sh} = \frac{E_{tot}}{p} \times \frac{\ln(E_{presh})}{\ln(E_{ave})} \quad (4)$$

where E_{tot} is the total energy deposited in the shower detector, p the particle's momentum, E_{presh} the energy deposited in the front layer and E_{ave} the average energy deposited by an electron with momentum p. The quality of the particle identification in the HRS-R shower detector is demonstrated in Fig. 13. The combination of the gas Cherenkov and shower detectors provides a pion suppression above 2 GeV/c of a factor of 2×10^5,

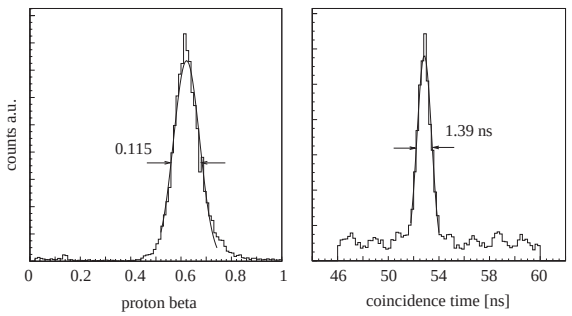

Fig. 11. Velocity distribution (left) in units of $\beta = v/c$ for protons and the coincidence time spectrum (right) between the two HRS, as measured with the two scintillator planes. The small peaks in the right figure show the time structure of the primary electron beam.

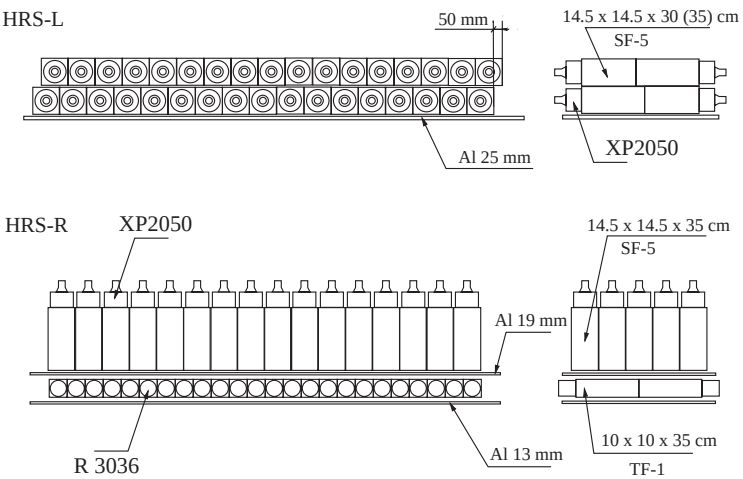

Fig. 12. Schematic lay-out of part of the shower detectors in HRS-L (top) and HRS-R (bottom). Particles enter from the bottom of the figure.

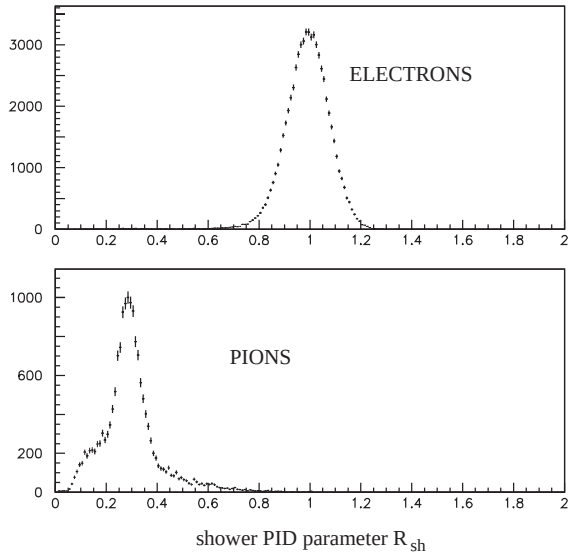

Fig. 13. The response function (defined in the text) of the HRS-R shower detector for pions and electrons at a momentum of 1.6 GeV/c.

with a 98% efficiency for electron selection in the HRS-R.

There are three aerogel Cherenkov counters available with various indices of refraction, which can be installed in either spectrometer and allow a clean separation of pions, kaons and protons over the full momentum range of the HRS spectrometers. The first counter (AM) contains hygroscopic aerogel[20] with a refraction index of 1.03 and a thickness of 9 cm. The aerogel is continuously flushed with dry CO_2 gas. It is viewed by 26 PMTs (Burle 8854). For high-energy electrons the average number of photo-electrons is about 7.3 [24].

The next two counters (A1 and A2) [25] are diffusion-type aerogel counters. The diffusion technique for light collection in aerogel Cherenkov detectors was evaluated in Refs. [26–28]. A1 has 24 PMTs (Burle 8854). The 9 cm thick aerogel radiator used in A1[21] has a refraction index of 1.015, giving a threshold of 2.84 (0.803) GeV/c for kaons (pions). The average number of photo-electrons for GeV electrons in A1 is $\simeq 8$ (see Fig. 14). The A2 counter has 26 PMTs (XP3372B1, see footnote 19). The aerogel in A2 (see footnote 21) has a refraction index of 1.055, giving a threshold of 2.8 (0.415) GeV/c for protons (pions). The thickness of the aerogel radiator in A2 is 5 cm, producing an average number of about 30 photo-electrons for GeV electrons [25].

[20] Airglass AB, BOX 150, 245 22 Staffanstorp, Sweden.

[21] Matsushita Electric Works, www.mew.co.jp.

3.6. The Focal Plane polarimeter

The Focal Plane polarimeter in Hall A measures the polarization of recoil protons over a wide range of electron scattering experiments. Following momentum analysis and focusing in the spectrometer, the protons are scattered in the focal plane region by an analyzer. If the protons are polarized transverse to the momentum direction, an azimuthal asymmetry results from the spin–orbit interaction with the analyzing nucleus. The measured asymmetry in the focal plane along with the spin-transfer matrix of the spectrometer is used to determine the polarization of the protons at the initial reaction vertex.

A detailed description of the polarimeter is given in Ref. [29]. The general design of the polarimeter follows that of existing devices at other intermediate energy facilities. As shown in Fig. 8, a set of front straw chambers measures the trajectory of a proton into the analyzer; the outgoing trajectory is determined by a set of rear straw chambers. The front chambers are interleaved with the gas Cherenkov and second scintillator plane, due to space constraints in the detector stack.

The standard analyzer is carbon, with cost, safety, and efficiency considerations outweighing the reduction in analyzing power available compared to hydrogen. The analyzer, made of high purity graphite, has a maximum thickness of 513 mm. The thickness is varied below proton momenta of 1.5 GeV/c in order to keep the Coulomb scattering cone narrower than 3°. The thickness variation is implemented through five remote-controlled slabs of increasing thickness (19, 38, 76, 152, and 228 mm). At proton momenta above 2.5 GeV/c, carbon becomes less efficient as an analyzer. An alternate polyethylene analyzer was used at the higher momenta in the second G_E^p experiment [30].

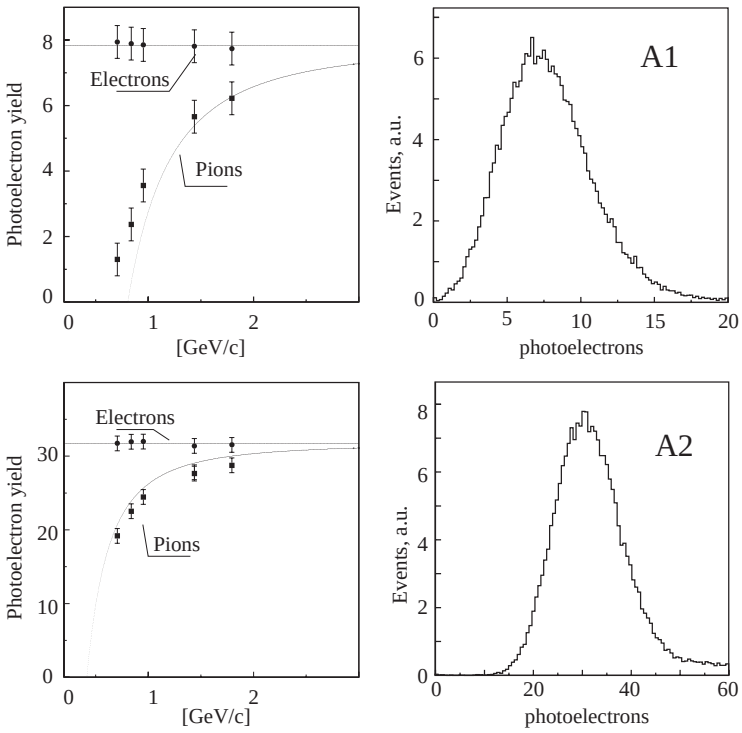

Fig. 14. The photo-electron yield vs particle momenta for A1 and A2 detectors (left) and examples of spectra for 2 GeV electrons (right). The curves indicate the expected photoelectron yield for the different particles as a function of momentum.

The dimensions of the rear straw chambers were chosen to be large enough that the geometrical efficiency is nearly 100% for a scattering angle up to 20° for the full acceptance of the HRS. The beam envelope in the region of the analyzer is about 2 m wide in x, the momentum dispersion direction, and 0.5 m wide in y, the transverse horizontal direction, with a divergence of several degrees in each direction. This leads to a rear chamber active area of about 2.8 m × 1.4 m. With these wire chamber sizes, scattering angles up to 70° are within the acceptance of the polarimeter with a slightly reduced geometrical efficiency at the larger angles.

Studies indicated that the design goal of instrumental asymmetries less than 0.005 could be reached with a chamber spatial resolution of ~0.25 mm, and an alignment to ~0.3 mrad. In order to minimize cost and optimize performance, drift chambers consisting of 10 mm diameter straw tubes were chosen due to the large size of the chambers. The designs of the individual straw tubes, and the end pieces associated with them, were based on the design used in the Brookhaven EVA cylindrical detector [31]. Because the chamber dimensions are much larger in the x than in the y direction, wires are generally oriented along the U and V directions, at 45° angles to the x and y directions to minimize wire lengths. To provide redundancy, the four FPP chambers are constructed with 3 U and 3 V planes. An exception was made for chamber 3, the first of the two rear chambers. Chamber 3 was constructed with 2 U, 2 V, and 2 X planes, so that multiple tracks could be analyzed with the stereo information. For the rear chambers, the straw package was stiffened by a sandwich construction, with straws inside and faces made of 0.036 mm thick three-ply carbon

fiber, glued together by a combination of UV-setting glues and long setting-time two-component epoxy.

A mixture of 62% argon and 38% ethane is run at a constant flow through every straw of the front and the back chambers. A positive high voltage of $\sim$1.9 kV is applied to the wire in the center of each straw. The anode gain per primary ionization is roughly 10^5. The anode signal is fed to read-out cards mounted on the chamber frames. To reduce cost, groups of eight wires are multiplexed in the read-out cards which produce differential output signals of amplitude 0.1 V. Level-shifter boards located away from the chambers, near the TDCs, convert these signals to ECL levels for input into the LeCroy 1877 [27] multi-hit TDCs. Through this scheme the design goal of $\sim$1% dead time at a 1 MHz rate is achieved at a reduced channel cost.

Incident and scattered particle trajectories are determined by identifying clusters of hits in the straw planes and fitting straight lines with the best χ^2 using the analysis code ESPACE (Section 8.1). Typical detection efficiencies achieved are about 98% per straw plane. Spatial alignment offsets for the straw planes are determined by straight-throughs without the carbon analyzer, and using the VDC tracks as reference. The interaction vertex and the polar and azimuthal scattering angles are determined from the tracks. The spin-transfer matrix elements of the spectrometer were determined by modelling the spectrometer in codes SNAKE [9] and COSY [32] using the measured magnetic field maps for the different elements.

Typically, events with a polar angle greater than 5° in the carbon analyzer are selected as good FPP events. The efficiency of the polarimeter, i.e. the fraction of total events accepted as good FPP events, is shown in Fig. 15 as a function of the proton energy. The carbon thickness was increased as a function of proton momentum from 38 mm at 0.59 GeV/c to 494 mm at 1.55 GeV/c; for higher momenta the thickness was kept constant at 494 mm. The solid squares in Fig. 15 are for a scattering angle cut from 5° to 20° and the solid circles represent the full acceptance up to 70°. As seen in the data, the scattering efficiency in the full acceptance of the FPP is considerably higher. Calibration of the inclusive analyzing power of the

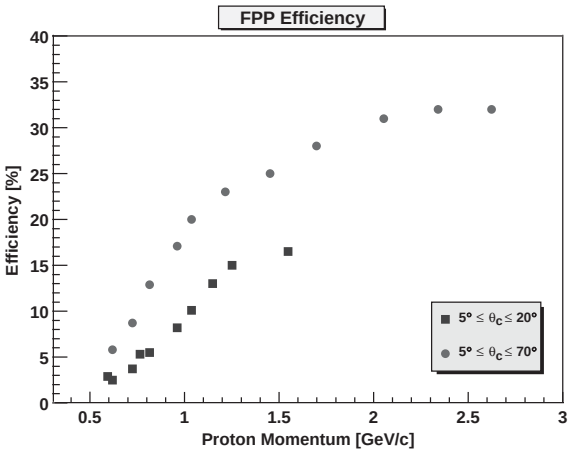

Fig. 15. The scattering efficiency of the FPP as a function of proton momentum for scattering angles from 5° to 20° (solid squares) and for 5° to 70° (solid circles). The thickness of the analyzer was varied with momentum as described in the text.

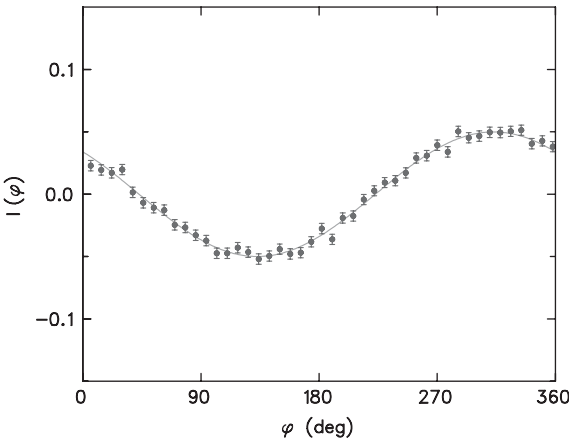

Fig. 16. The azimuthal distribution of protons scattered in the FPP in ep elastic scattering with 4.6 GeV incident electron energy and $Q^2 = 3.5$ (GeV/c)^2.

carbon analyzer and of instrumental asymmetries was done with the elastic ep reaction [3,30]. Azimuthal asymmetries measured for elastic ep scattering at $Q^2 = 3.5$ (GeV/c)^2 are shown in Fig. 16. Typical instrumental asymmetries measured are about 0.005. A Fourier analysis of this measured asymmetry provides a direct measure of the analyzing power and the ratio of the magnetic

to electric form factor of the proton. The average inclusive analyzing power for carbon, with angular acceptance from 5° to 20° (solid squares) and 5° to 70° (solid circles), is shown in Fig. 17.

4. Beamline

The instrumentation along the beamline (shown in Fig. 18) consists of various elements necessary to transport the electron beam onto the target and into the dump, and to measure simultaneously the relevant properties of the beam. The resolution and accuracy requirements are such that special attention is paid to the control and determination of the beam energy, current and polarization, and also to the position, direction, size and stability of the beam at the Hall A target location.

Table 2 lists all the beam parameters monitored along the beamline and the associated instrumentation. In nearly all cases, two or more independent methods are available to determine and monitor the various parameters in order to provide confidence in the absolute measurements and redundancy if any of the instrumentation should fail during a run. The beam parameters listed in Table 2 are determined and monitored at a level which in most cases meets or exceeds the needs of the approved experiments. The various elements along the beamline are listed and described in detail in the Hall A Operations Manual [33].

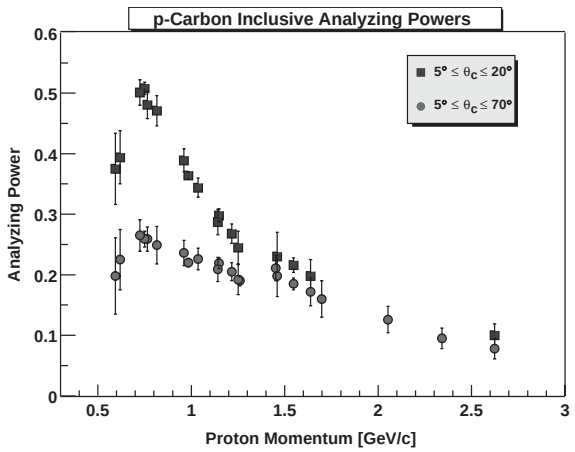

Fig. 17. The average analyzing power of the carbon analyzer as a function of proton momentum. Solid squares are averages over scattering angles from 5° to 20° and the solid circles for those from 5° to 70°.

4.1. Basic beamline

The beam entrance channel consists of 63.5 mm inner diameter stainless steel tubing connected with conflat flanges. Through magnets the inner diameter of the tubing is restricted to 25.4 mm.

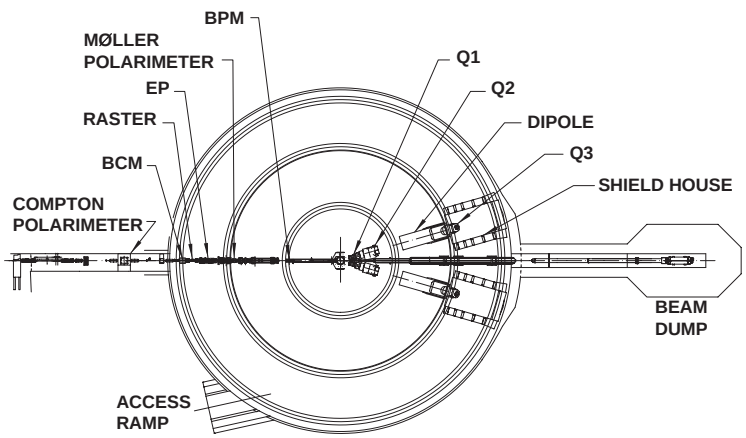

Fig. 18. Schematic layout of Hall A, indicating the location of the Compton and the Møller polarimeters, the raster, the EP energy measurement system, the beam current monitors (BCM) and the beam position monitors (BPM) upstream of the target. Also indicated are the locations of the components of one of the high-resolution spectrometers (Q1, Q2, dipole, Q3 and shield house) and of the beam dump and the truck access ramp.

Table 2
Overview of the methods available for the determination of beam parameters

Parameter	Method		Accuracy	Comments
Energy	Arc	Absolute	2×10^{-4}	Invasive
			5×10^{-4}	Non-invasive
		Relative	1×10^{-4}	Non-invasive
	eP	Absolute	2×10^{-4}	Invasive
Energy width	OTR		$\frac{\Delta E}{E} \sim 1 \times 10^{-5}(\sigma)$	Non-invasive
Current ($\geqslant 1$ μA)	2 RF Cavities	Absolute	$\leqslant 5 \times 10^{-3}$	Non-invasive
Position (at target)	2 BPM/Harp	Absolute	140 μm	x, y on line
Direction (at target)	2 BPM/Harp	Absolute	30 μrad	θ, ϕ on line
Stability (at target)	Fast Feedback		$\leqslant 720$ Hz motion	
	Position		$\leqslant 20$ μm (σ)	
	Energy		$\leqslant 1 \times 10^{-5}$ (σ)	
Polarization	Møller	Absolute	$\frac{\Delta P}{P} \approx 3\%$ ($\Rightarrow 2\%$)	Invasive
	Compton	Absolute	$\frac{\Delta P}{P} \approx 3\%$ ($\Rightarrow 1.4\%$)	Non-invasive

The third column indicates whether a method provides an absolute or relative result. In the fourth column a σ indicates that the accuracy given is the width of an assumed Gaussian distribution. An arrow indicates the expected future accuracy. In the fifth column non-invasive implies that the measurement does not affect the quality of the main experiment.

The beamline is segmented into several sections isolated by vacuum valves with each section having a roughing port and pumped by an ion pump. The beamline is maintained at a vacuum pressure $\leqslant 10^{-6}$ Torr. The beam diagnostic elements consist of transmission-line position monitors, current monitors, superharps, viewers, loss monitors and optical transition radiation (OTR) viewers. The beam optics elements consist of focussing quadrupoles, sextupoles and corrector magnets. The standard beam delivery optics tune to Hall A is an achromatic tune (zero dispersion) with double focussing at the target location. Beam spot sizes of 100–200 μm (rms value) are routinely available. Tunes which provide a dispersed or defocussed beam at the target location are also available. A fast rastering system (17–24 kHz) located 23 m upstream of the target position allows the beam to be rastered over several mm's in both directions at the target.

The beam exit channel consists of a thin-walled aluminum spiral corrugated pipe of welded construction able to hold a vacuum of 10^{-4} Torr. It is made up of several sections of increasing diameter starting with the smallest section (152.4 mm diameter with a 107 μm wall thickness) and ending with the largest diameter section (914 mm diameter with a 4.2 mm wall thickness). The assembly is supported by eight light H-shaped stands. The larger diameter sections have four aluminum channels welded to their sides to prevent a possible collapse under vacuum load. The exit face of this corrugated pipe is located 3 m inside the dump tunnel. It has a 305 mm diameter port and is connected to a beam diffuser. The diffuser, consisting of two 6.3 mm thick beryllium foils with water flowing between them, diffuses the beam over the beam dump surface located 23 m inside the exit dump tunnel. The beam dump [34] is designed to operate at a maximum beam power of 900 kW and a maximum beam current of 190 μA.

4.2. Beam position and direction

To determine the position and direction of the beam at the target location, two Beam Position

Monitors (BPMs) are located 7.524 m and 1.286 m upstream of the target. The standard difference-over-sum technique is then used to determine the relative position of the beam to within 100 μm for currents above 1 μA [35]. The absolute position of the beam can be determined from the BPMs by calibrating them with respect to wire scanners (superharps) which are located adjacent to each of the BPMs (7.353 and 1.122 m upstream of the target). The wire scanners are surveyed with respect to the Hall A coordinates at regular intervals and the results are reproducible at the level of 200 μm. The position information from the BPMs, which has to be calibrated independently of the scanner data, can be recorded in two different ways:

1. The position averaged over 0.3 s is logged into the EPICS (see Section 6) database with 1 Hz updating frequency and injected asynchronously into the data-stream every 3–4 s.

2. Event-by-event information from the BPMs is recorded in the CODA (see Section 7) data stream from each of the 8 BPM antennas (2×4).

4.3. Current and charge calibrations

The Beam Current Monitor (BCM) of Hall A is designed for a stable, low-noise, non-interfering beam current measurement. It consists of an Unser monitor, two RF cavities, associated electronics and a data-acquisition system. The cavities and the Unser monitor are enclosed in a temperature-stabilized box to improve magnetic shielding. The box is located 25 m upstream of the target location. The down converters and the Unser front-end electronics are located inside the hall. The temperature controller, the Unser back-end electronics and its calibration current source, the cavity's RF unit (housing the RMS-to-DC converter board) and all multimeters, the VME crate and computers are located in the control room. In addition to the Unser monitor, a cavity monitor and a Faraday Cup at the injector section [36] of the main accelerator are also used to provide an absolute reference during calibration runs.

The Unser monitor is a Parametric Current Transformer which provides an absolute reference [37]. The monitor is calibrated by passing a known current through a wire inside the beam pipe and has a nominal output of 4 mV/μA. It requires extensive magnetic shielding and temperature stabilization to reduce noise and zero drift. As the Unser monitor's output signal drifts significantly on a time scale of several minutes, it cannot be used to continuously monitor the beam current.

The two resonant RF cavity monitors on either side of the Unser Monitor are stainless steel cylindrical high-Q (~ 3000) waveguides which are tuned to the frequency of the beam (1.497 GHz) resulting in voltage levels at their outputs which are proportional to the beam current. Each of the RF output signals from the two cavities is split into two parts (to be sampled or integrated).

For the sampled data, one of the amplifier outputs is sent to a high-precision digital AC voltmeter (HP 3458A, see footnote 12). This device provides, once every second, a digital output which represents the RMS of the input signal during that second. The resulting number is proportional to the beam charge accumulated during the corresponding second (or, equivalently, the average beam current for that second). Signals from both cavities' multimeters, as well as from the multimeter connected to the Unser, are transported through GPIB ports to a computer where they are recorded every 1–2 s via the data-logging process. They are also combined into the CODA data stream at regular intervals, typically every 2–5 s.

For the integrated data, the other amplifier output is sent to an RMS-to-DC converter, consisting of a 50 kHz bandpass filter to eliminate noise, which produces an analog DC voltage level. This level drives a Voltage-To-Frequency (VTOF) converter whose output frequency is proportional to the input DC voltage level. These signals are then fed to 200 MHz VME scalers, the output of which is injected into the data stream along with other scaler information. These scalers simply accumulate during the run, resulting in a number which is proportional to the time-integrated voltage level, and therefore more accurately represents the total beam charge. The regular RMS to DC output is linear for currents from about 5 μA to well above 200 μA. A set of amplifiers has been introduced with gain factors

of 3 and 10, to extend the non-linear region to lower currents at the expense of saturation at high currents. Hence, there is a set of three signals coming from each BCM. These six signals are fed to scaler inputs of each spectrometer, providing a redundancy of twelve scaler outputs for determining the charge during a run.

Each of these scaler outputs is calibrated during calibration runs. During a typical calibration run, the current is ramped between zero and the maximum current through at least five cycles (more for greater accuracy), dwelling at each step for 60–90 s. This allows the drift of the Unser monitor to be accurately taken into account. A CODA run is taken simultaneously in order to obtain the charge scalers. Thus, the two BCM monitors are calibrated with the Unser at the same time as the charge monitors. This calibration is performed every 2–3 months and the results are stable within $\pm 0.5\%$. Following these procedures, the charge for a data-taking run for a physics experiment can be determined down to a current of 1 μA with an accuracy of $\leqslant 0.5\%$.

4.4. Absolute energy measurements

The energy of the beam is measured absolutely by two independent methods [38]. The Arc method determines the energy by measuring the deflection of the beam in the arc section of the beamline. The nominal bend angle of the beam in the arc section is 34.3°. The measurement is made when the beam is tuned in dispersive mode in the arc section. The momentum of the beam (p in GeV/c) is then related to the field integral of the eight dipoles ($\int \vec{B} \cdot \vec{dl}$ in Tm) and the net bend angle through the arc section (θ in radians) by

$$p = k \frac{\int \vec{B} \cdot \vec{dl}}{\theta} \tag{5}$$

where $k = 0.299792$ GeV rad T^{-1} m^{-1}/c.

The method consists of two simultaneous measurements, one for the magnetic field integral of the bending elements (eight dipoles in the arc), based on a reference magnet (9th dipole) measurement, and the actual bend angle of the arc, based on a set of wire scanners. Specific instrumentation for the Arc method [39] includes the scanners, an absolute angle measurement device, and an absolute field integral measurement device for the reference magnet. Table 3 gives the error breakdown ($\Delta E/E$) for two beam energies in terms of the standard deviation of the quadratic sum of the errors.

Table 3
Systematic uncertainty for the Arc Energy Method for two values of the beam energy

	$E = 0.5$ GeV	$E = 4.0$ GeV
Bend angle	2.2×10^{-5}	2.2×10^{-5}
Field integral	1.2×10^{-4}	6.4×10^{-5}
Energy	1.2×10^{-4}	6.8×10^{-5}

The first row gives the contribution to the total error from the determination of the bend angle in the beam switch yard, the second row from that of the field integral in each of the eight dipole magnets. The third row lists the expected total error.

The eP method [38,40] utilizes a stand-alone device along the beamline located 17 m upstream of the target. In this method, the beam energy E is determined by measuring the scattered electron angle θ_e and the recoil proton angle θ_p in the $^1\mathrm{H}(\mathrm{e},\mathrm{e}'\mathrm{p})$ elastic reaction according to the kinematic formula:

$$E = M_p \frac{\cos(\theta_e) + \sin(\theta_e)/\tan(\theta_p) - 1}{1 - \cos(\theta_p)} + O(m_e^2/E^2) \tag{6}$$

in which M_p denotes the mass of the proton and m_e that of the electron. The schematic diagram of the eP system is presented in Fig. 19. Two identical arms, each consisting of an electron and a corresponding proton detector system, made up of a set of 2×8 silicon micro-strip detectors in the reaction plane, are placed symmetrically with respect to the beam along the vertical plane. Simultaneous measurements of the beam energy with both arms result in cancellation, to first order, of uncertainties in the knowledge of the position and direction of the beam.

Repeated measurements of the beam energy with both methods show good agreement with each other within their respective uncertainties ($\leqslant 3 \times 10^{-4}$) except at around 3 GeV as shown in Fig. 20. Because for different energy ranges,

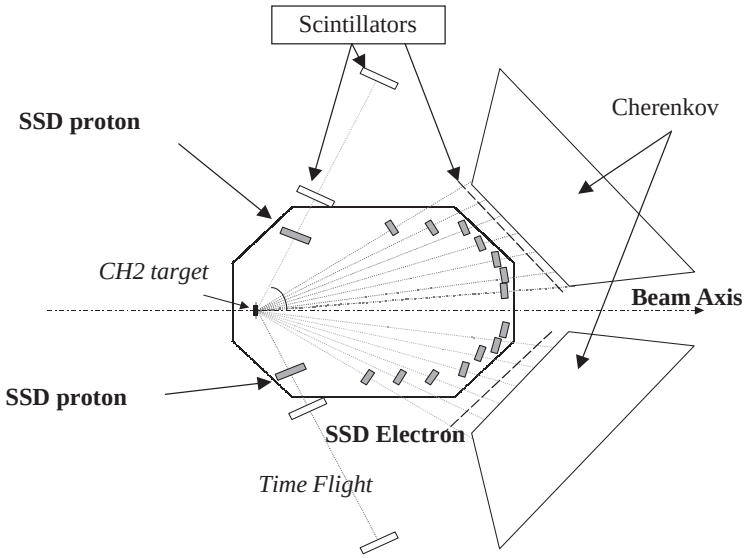

Fig. 19. Schematic layout of the eP energy measurement system, showing the arrangement of its components, the polyethylene (CH2) target, the Cherenkov detectors, the silicon-strip detectors (SSD) for protons and electrons and the scintillator detectors, used for time-of-flight measurements.

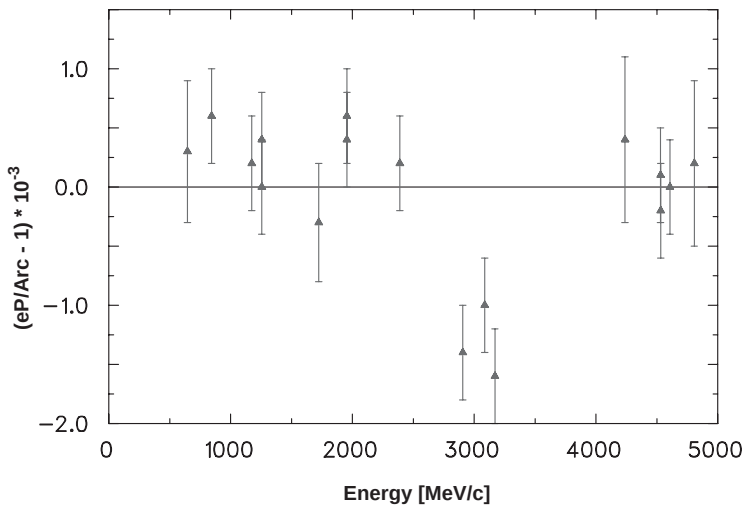

Fig. 20. A comparison of energy measurements with the Arc and the eP system as a function of the electron beam energy.

different microstrip detectors are used for the eP method, it is conjectured that this discrepancy at around 3 GeV is due to the misalignment of one particular microstrip detector in the eP setup. At present, there is an effort to understand the sources of these discrepancies at around 3 GeV.

4.5. Beam polarimetry

An important part of the experimental program in Hall A uses a polarized electron beam, with a typical beam polarization of 75–85%. In order to measure the polarization of the electron beam

delivered to the hall, the beamline is equipped with two polarimeters, whose functions are partly overlapping and partly complementary.

4.5.1. Møller polarimeter

A Møller polarimeter exploits the process of Møller scattering of polarized electrons off polarized atomic electrons in a magnetized foil $\vec{e}^- + \vec{e}^- \to e^- + e^-$. The reaction cross section depends on the beam and target polarizations P^{beam} and P^{target} as

$$\sigma \propto \left[1 + \sum_{i=X,Y,Z} (A_{ii} \cdot P_i^{\text{target}} \cdot P_i^{\text{beam}})\right] \tag{7}$$

where $i = X, Y, Z$ defines the projections of the polarizations [41]. The analyzing power A depends on the scattering angle in the CM frame, θ_{CM}. Assuming that the beam direction is along the Z-axis and that the scattering happens in the ZX plane:

$$A_{ZZ} = -\frac{\sin^2\theta_{\text{CM}}(7 + \cos^2\theta_{\text{CM}})}{(3 + \cos^2\theta_{\text{CM}})^2},$$

$$A_{XX} = -\frac{\sin^4\theta_{\text{CM}}}{(3 + \cos^2\theta_{\text{CM}})^2}, \quad A_{YY} = -A_{XX}. \tag{8}$$

At $\theta_{\text{CM}} = 90^\circ$ the analyzing power has its maximum value $A_{ZZ}^{\max} = 7/9$. A beam polarization transverse to the scattering plane also leads to an asymmetry, though the analyzing power is lower: $A_{XX}^{\max} = A_{ZZ}^{\max}/7$. The main purpose of the polarimeter is to measure the longitudinal component of the beam polarization.

The Møller polarimeter uses a ferromagnetic foil, magnetized in a magnetic field of about 24 mT along its plane, as a target of polarized electrons. The target foil can be tilted at various angles to the beam in the horizontal plane, providing a target polarization that has both longitudinal and transverse components. The spin of the incoming electron beam may have a transverse component due to precession in the accelerator and in the extraction arc. The asymmetry is measured at two target angles of about $\pm 20^\circ$ and the average is taken. Because the transverse contributions have opposite signs for these target angles, the transverse contributions cancel in the average. Additionally, this method reduces the impact of uncertainties in the target angle measurements. At a given target angle two sets of measurements with opposite directions of the target polarization are taken. Averaging the results helps to cancel some of the false asymmetries, such as that coming from the residual helicity-driven asymmetry of the beam flux. The target polarization is derived from foil magnetization measurements. For a supermendur foil[22] used in the 1998–2000 period a polarization of $7.95 \pm 0.24\%$ was obtained. The error includes the uncertainties in the spin–orbit correction as well as in the magnetic flux measurements, in the foil inhomogeneity and in the sample size.

The Møller scattering events are detected with the help of a magnetic spectrometer (see Fig. 21) consisting of a sequence of three quadrupole magnets and a dipole magnet. The spectrometer selects electrons scattered close to the horizontal plane, in a kinematic range of about $75^\circ < \theta_{\text{CM}} < 105^\circ$ and $-5^\circ < \phi_{\text{CM}} < 5^\circ$, where ϕ_{CM} is the azimuthal angle. The non-scattered electron beam passes through a 4 cm diameter hole in a vertical steel plate 6 cm thick, positioned at the dipole midplane, which serves as a collimator for the scattered electrons and as a magnetic shield for the beam. The polarimeter can be used at beam energies from 0.8 to 6 GeV, by setting the appropriate fields in the magnets. The lower limit is defined by the acceptance of the polarimeter to the Møller electron pairs, which drops at low energies. The upper limit depends mainly on the magnetic shielding of the beam area inside the dipole.

The detector consists of lead-glass calorimeter modules, split into two arms in order to detect two scattered electrons in coincidence. The helicity-driven asymmetry of the coincidence counting rate (typically about 10^5 s^{-1} at a 0.5 μA beam current) is used to derive the beam polarization. The ratio of the singles rate to the coincidence rate is about two for beam energies higher than 1.5 GeV, while it rises to five at the lowest beam energy used, 0.8 GeV. A comparison of the asymmetries measured with the single-arm signal and the coincidence indicates that about 30% of the single-arm

[22] Supermendur is a 49% Fe, 49% Co, 2% Va alloy.

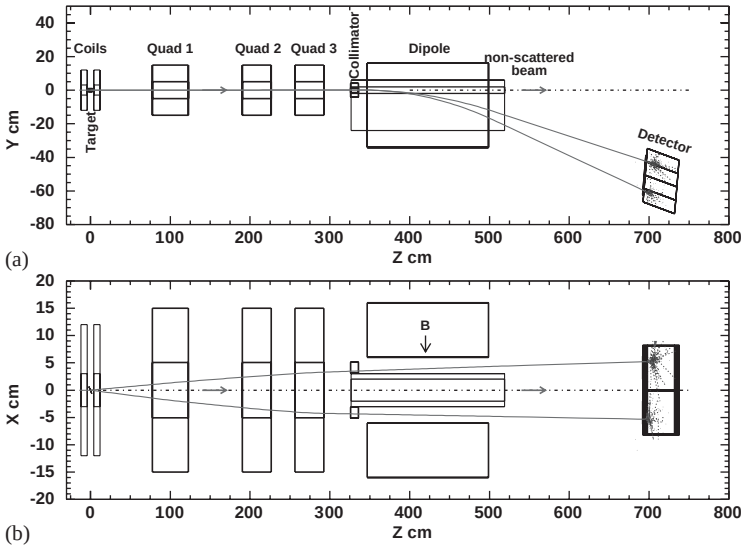

Fig. 21. Layout of the Møller polarimeter, (a) presents a side view while, (b) presents a top view. The trajectories displayed belong to a simulated event of Møller scattering at $\theta_{CM} = 80^\circ$ and $\phi_{CM} = 0^\circ$, at a beam energy of 4 GeV.

rate is caused by non-Møller sources, consistent with predictions of radiative Mott scattering on the target nuclei. The estimated background level of the coincidence rate is below 0.5%.

The polarization measurements with the Møller polarimeter are invasive and one measurement typically takes an hour, providing a statistical accuracy of about 0.2%.

4.5.2. Compton polarimeter

The Compton polarimeter, utilizing the process of Compton scattering, was designed to measure the beam polarization concurrently with experiments running in the hall to a 1% statistical error within an hour [42]. The polarization is extracted from the measurement of the counting rate asymmetry for opposite beam helicities in the scattering of a circularly polarized photon beam by the electron beam.

Installed at the entrance of the hall, the Compton polarimeter consists of a magnetic chicane, a photon source, an electromagnetic calorimeter, and an electron detector as shown in Fig. 22. The electron beam is deflected vertically by the four dipoles of the chicane and crosses the photon beam at the Compton interaction point. After interaction, the backscattered photons are detected in the calorimeter [43] and the electrons in the silicon strip electron detector located a few mm above the primary beam in front of the fourth dipole. Electrons that did not interact exit the polarimeter and reach the target. A fast front-end electronics and data-acquisition system is required to collect data at rates of up to 100 kHz.

A resonant Fabry–Pérot cavity is used as a power amplifier for the photon beam [44]. This monolithic cavity, 85 cm long, uses two high-finesse mirrors ($\mathscr{F} = 26,000$) to amplify a primary 230 mW CW Nd:YaG laser beam ($\lambda = 1064$ nm). The circular polarization of the photon beam can be reversed using a rotatable quarter-wave plate. To reach and maintain the maximum amplification of the photon density a feedback loop insures that the laser frequency is locked to that of the cavity. This locking procedure is fully automatic and requires only a few seconds. An amplification factor of 7300 has been measured, corresponding to a photon beam power of 1680 W inside the cavity. The circular polarization was measured to be $-99.3\% \pm 0.6\%$ for negative photon helicity states and $99.9\% \pm 0.6\%$ for positive ones. Both

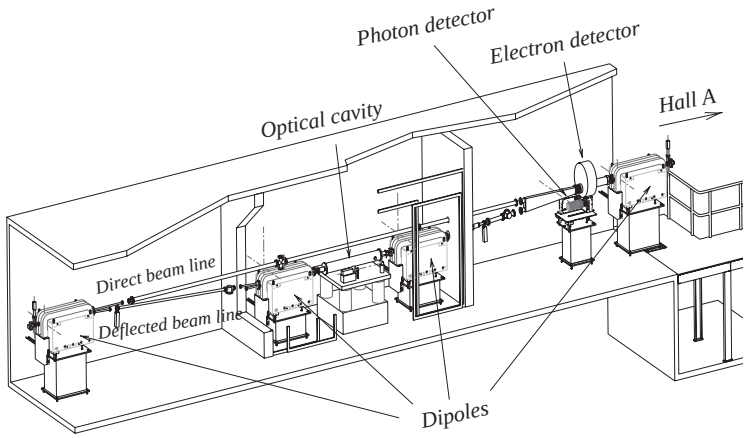

Fig. 22. Schematic layout of the Compton polarimeter, showing the four dipoles of the chicane, the optical cavity and the photon and electron detector.

the optical power and polarization remain stable for more than 10 h.

In order to maximize the Compton luminosity, the crossing angle between the two beams has to be as small as possible. At the design crossing angle of 23 mrad the mirrors are about 5 mm away from the electron beam. Compton events were clearly detected by scanning the vertical position of the electron beam, varying the field in the dipoles, until both beams cross at the center of the cavity. Once the position of the electron beam has been tuned to maximize the Compton interaction rate, data are recorded for both photon beam polarizations [42]. Either single electrons, single photons or coincidences can trigger the acquisition. The background contribution is measured during periods of laser beam off. A background/signal ratio of 0.05 has been routinely obtained.

The energy of the scattered particles is reconstructed from the position of the electrons in the micro-strip planes and from the amount of light collected in the photon calorimeter. A nice feature of the coincidence mode is that the set of micro-strips of the electron detector can operate as a photon energy tagger allowing an on-line determination of the response function of the calorimeter. This method is the most efficient so far in terms of the control of the systematic errors associated with the resolution and calibration of the detectors.

At 4.5 GeV and a 40 μA beam current, an asymmetry, P^{raw}, of 5.5% has been measured with a relative statistical accuracy, $\Delta P^{\mathrm{raw}}/P^{\mathrm{raw}}$, of about 1% within 30 min [45].

4.5.3. Systematic uncertainties and polarimeters cross calibration

The most important systematic uncertainties of the two polarimeters are different. The dominant uncertainty of the Møller polarimeter comes from the uncertainty in the target polarization, while that of the Compton polarimeter comes from its low analyzing power. Another uncertainty comes from the fact that the Møller polarimeter has to use a low beam current (0.5 μA, typically). The current is reduced at the injector, either by attenuating the laser light or with a slit at the chopper, each of which might change the beam polarization. In contrast, the Compton polarimeter is used at the same current as the experiments. There is no beam interference in this technique, but the figure of merit goes like E^2_{beam} leading to less accurate measurements at low energy. At typical CEBAF energies of a few GeV the main uncertainties come from the knowledge of the detectors' calibration and resolution in the determination of the mean analyzing power. In the measurement of the Compton asymmetry, special care has to be taken to minimize the sensitivity to helicity-correlated beam parameters, like the beam

Table 4
Breakdown of the systematic uncertainties for the Møller polarimeter

Origin	Dilution factor	Relative error
Target polarization	0.079	3.0%
Target angle	0.94	0.5%
Analyzing power	0.76	0.3%
Transverse polarization	—	0.3%
Non-polarized background	—	<0.5%
Electron intra-atomic motion [92]	—	<0.4%
Dead-time	—	0.3%
Low/high beam current	—	1.0%
Observed fluctuations	—	1.0%
Total		3.4%

The dilution factor represents the factor used to divide the raw asymmetry in order to obtain the polarization, if such a correction is done. The last line presents the sum of the errors in quadrature.

Table 5
Typical Compton polarimeter systematic errors at 4.5 GeV, for a 1 h run

Origin	Dilution factor	Relative error
Photons' polarization	0.995	0.45%
Analyzing power	0.055	0.95%
Beam position and angle	—	0.45%
Dead-time	—	0.10%
Background	0.95	0.05%
Total		1.2%

position. The background depends critically on the beam tune. The Møller polarimeter is insensitive to these kinds of uncertainties. The systematic errors for the Møller and Compton polarimeters are presented in Tables 4 and 5, respectively.

The polarimeters have been carefully cross-calibrated under conditions which minimized possible systematics associated with the value of the beam current. The polarization measured was $72.7 \pm 0.5 \pm 1.2\%$ by the Compton and $75.12 \pm 0.13 \pm 2.5\%$ by the Møller polarimeter, where the first error is statistical and the second is systematic. The relative difference (3.2%) in the two polarization measurements is consistent within the systematic uncertainties.

5. The target system

5.1. The scattering chamber

The standard scattering vacuum chamber is constructed out of several rings 1037 mm in diameter, supported on a 607 mm diameter central pivot post. The stainless-steel base ring has one vacuum pump-out port and other ports for viewing and electrical feed-throughs. The middle ring is made out of aluminum and located at beam height with 152 mm vertical cutouts on each side of the beam over the full angular range ($12.5^\circ \leqslant \theta \leqslant 167.5^\circ$). The cutouts are covered with a pair of flanges with thin (0.38 mm) aluminum foils. It also has entrance and exit beam ports. The upper ring is used to house the cryotarget.

5.2. Cryogenic targets

The cryogenic target system is mounted inside the scattering chamber along with sub-systems for cooling, gas handling, temperature and pressure monitoring, target control and motion, and an attached calibration and solid target ladder.

The basic cryogenic target has three independent target loops: a liquid hydrogen (LH_2) loop, a liquid deuterium (LD_2) loop and a gaseous helium loop. Each of the two liquid loops has two aluminum cylindrical target cells mounted on the target ladder. The cells are 63.5 mm in diameter and can be either 4 or 15 cm long. The sidewalls of the cells are 178 μm thick, with entrance and exit windows approximately 71 and 102 μm thick, respectively. The upstream window consists of a thick ring holder with an inner diameter of 19 mm, large enough for the beam to pass through. The gaseous helium target can be filled with either ^{3}He or ^{4}He gas. The helium loop has a single vertical cylindrical cell, also made out of aluminum. The cell has a diameter of 10.4 cm (which defines the target length) and a wall thickness of 0.33 mm. The operating temperature and pressure of the

LH_2 (LD_2) target are 19 K (22 K) and 0.17 MPa (0.15 MPa), with a density of about 0.0723 g/cm^3 (0.167 g/cm^3). The LH_2 and LD_2 targets are sub-cooled by 3 K. The nominal operating condition for ^{4}He is 6.3 K at 1.4 MPa, giving a density of about 0.13 g/cm^3, and for ^{3}He 6.3 K at 1.1 MPa, giving a density of about 0.07 g/cm^3. The targets are arranged in a vertical stack, which can be moved from one position to another by remote control. Besides the five target positions for the cryotargets (10 cm helium, 15 and 4 cm LH_2, and 15 and 4 cm LD_2), there are three dummy targets and five solid targets. The dummy targets, used to measure contributions from the windows, contain two thin pieces of aluminum, separated by a distance of 10 cm, 15 cm or 4 cm. The solid target ladder has five target positions, usually occupied by a BeO target, an empty target, a ^{12}C target and two special-purpose targets. The solid targets are usually not cooled.

The targets are cooled with helium supplied by the ESR. The helium is available at 15 K with a maximum cooling power of 1 kW, and at 4.5 K with a lower maximum cooling capacity near 600 W. To maximize the luminosity, beam currents up to 130 μA have been used on the liquid hydrogen and deuterium targets cooled with the 15 K helium, which is then returned at slightly over 20 K. In this configuration the beam heating alone deposits 700 W in the target, and the heat load approaches 1 kW upon adding the circulating fans and small heater required to stabilize the target's temperature. The maximum luminosity achieved is over 5×10^{38} cm^{-2}/s. For the gaseous helium target, 4.5 K coolant is used. The switch between the two liquid loops can be done in a few minutes, while a change between the liquid and gas target systems usually takes about eight hours since the target gas has to be cooled down from room temperature. The coolant supply is controlled with JT valves (one for each loop), which can be adjusted either remotely or locally.

The target loops are supplied with the target gas at room temperature, with each loop controlled by an independent gas panel. Because hydrogen and deuterium are highly flammable and highly explosive (expanding by a factor of 800 during evaporation), safety was a major consideration during the design and construction of the gas handling system.

To minimize the uncertainty in the target density, the pressure and temperature are monitored with pressure transducers at several locations with a typical precision on the pressure measurement of better than 0.34 MPa, which contributes less than 0.1% to the density uncertainty. The primary temperature sensors are LakeShore Cernox (see footnote 11), precision semiconductor sensors with a high radiation resistance. The precision of the temperature measurement is about 0.05 K, which contributes less than 0.1% uncertainty to the density. Two other types of temperature sensors are used as checks: vapor-pressure transducers and resistors.[23] Diode temperature sensors are used in the coolant lines. The resistor and diode sensors are read out with an Oxford Temperature Monitor Model ITC 501,[24] while the Cernox's are read out with an Oxford Temperature Control Model ITC 502. Low-power heaters, up to 60 W, are controlled by the ITC 502 to keep the temperature stable. High-power heaters, up to 1 kW, are used to keep the target temperature stable when the beam is off. The temperature control is automated by a PID feedback loop. All computer controls use the JLab standard EPICS system.

All target positions are surveyed before and after experiments. The motion during vacuum pump-down and cool-down is monitored and corrected in the position determination. The targets are usually centered to about 1 mm with a typical position precision of about 0.5 mm.

Because of its small size the beam spot can cause local damage to the target cell at high beam currents. To minimize this, the electron beam is usually rastered to a diameter of a few mm (Section 4.1). With rastered beam, the density fluctuations from beam heating are limited to a few percent at a beam current of 100 μA. The dependence of density fluctuations on the beam current, raster size and circulation speed of the target liquid or gas has been studied. Further

[23] Allen-Bradley, www.ab.com.

[24] Oxford Instruments Superconducting Technology, 600 Milik Street, PO Box 429, Carteret, NJ 07008-0429, USA.

details can be found in the documents on the cryotarget web-page [46] and in a separate NIM article [47].

5.3. The polarized ^{3}He target

The polarized ^{3}He target was constructed in 1998 for a program to study the neutron spin structure and form factors in Hall A. It was successfully used for the first two polarized ^{3}He experiments [4,48] in the fall of 1998 and winter of 1999, which studied the spin structure of the neutron, the generalized GDH sum rule and the neutron magnetic form factor in the low Q^2 region. After implementing improvements, two further experiments have studied the neutron spin asymmetry in the valence quark region [49] and the twist-3 structure function g_2 [50]. Two more experiments [51,52] have been approved. The study of the nucleon structure in the valence quark region and higher-twist effects are key experiments for the JLab 12 GeV upgrade [53].

5.3.1. Operating principles

The polarized ^{3}He target is based on the principle of spin exchange between optically pumped alkali-metal vapor and noble-gas nuclei [54]. The design is similar to that used in the SLAC E-142 experiment [55]. A central feature of the target is a sealed glass cell, which contains ^{3}He gas at a pressure of about 0.69 MPa. As shown in Fig. 23, the target cells have two chambers, an upper chamber in which the spin exchange takes place, and a lower chamber, through which the electron beam passes. In order to maintain the appropriate number density of alkali-metal (Rb) the upper chamber is kept at a temperature of 170–200°C using an oven constructed of Torlon [56], a plastic which can withstand high temperatures. At a density of 2.5×10^{20} atoms/cm^3, a lower cell length of 40 cm corresponds to a target thickness of 1×10^{22} atoms/cm^2.

The time evolution of the ^{3}He polarization can be calculated from a simple analysis of spin-exchange and ^{3}He nuclear relaxation rates [57]. Assuming the ^{3}He polarization

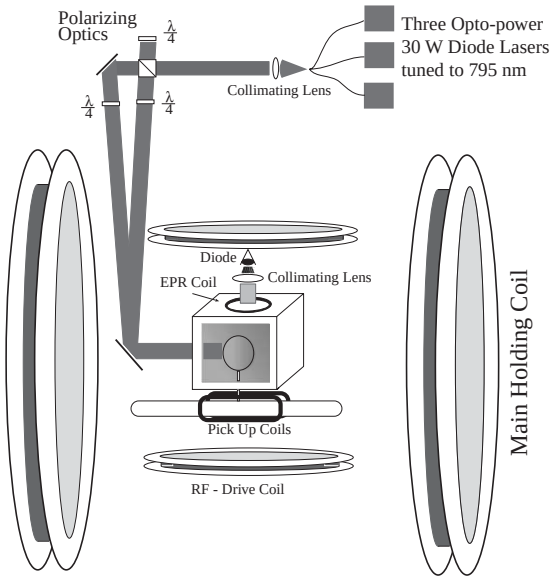

Fig. 23. Schematic layout of the spin-exchange polarized ^{3}He target. For clarity, only one set of Helmholtz coils is shown.

$$P_{^3\mathrm{He}} = 0 \text{ at } t = 0,$$

$$P_{^3\mathrm{He}}(t) = \langle P_{\mathrm{Rb}} \rangle \left(\frac{\gamma_{\mathrm{SE}}}{\gamma_{\mathrm{SE}} + \Gamma_{\mathrm{R}}} \right) (1 - \mathrm{e}^{-(\gamma_{\mathrm{SE}} + \Gamma_{\mathrm{R}})t}) \quad (9)$$

where γ_{SE} is the spin-exchange rate per ^{3}He atom between Rb and ^{3}He, Γ_{R} is the relaxation rate of the ^{3}He nuclear polarization through all channels other than spin exchange with Rb, and $\langle P_{\mathrm{Rb}} \rangle$ is the average polarization of a Rb atom. The present target is designed to operate with $1/\gamma_{\mathrm{SE}} = 8$ h.

From Eq. (9) it is clear that the best possible ^{3}He polarization is obtained by maximizing γ_{SE} and/or minimizing Γ_{R}. Maximizing γ_{SE} means increasing the Rb number density, which requires more laser power. The number of photons needed per second must compensate for the Rb spin relaxation. In order to achieve $1/\gamma_{\mathrm{SE}} = 8$ h, about 50 W of usable laser light at a wavelength of 795 nm is needed.

The rate at which polarization is lost, which is characterized by Γ_{R}, has four principal contributions. An average electron beam current of about 10 μA will result in a depolarization rate of $1/\Gamma_{\mathrm{beam}} = 45$ h [58]. From experience, target cells with an intrinsic rate of $1/\Gamma_{\mathrm{cell}} = 50$ h can be produced. This has two contributions, relaxation

that occurs during collisions of ^{3}He atoms due to dipole–dipole interactions [59], and relaxation that is presumably due largely to the interaction of ^{3}He atoms with the cell walls. Finally, relaxation due to inhomogeneities in the magnetic holding field are held to better than $1/\Gamma_{\Delta B} = 100$ h [60]. Collectively, under operating conditions, one would thus expect

$$\Gamma_R = \Gamma_{beam} + \Gamma_{cell} + \Gamma_{\Delta B} = 1/45\ \text{h} + 1/50\ \text{h} + 1/100\ \text{h} = 1/19\ \text{h}. \quad (10)$$

Thus, according to Eq. (9), the target polarization cannot be expected to exceed

$$P_{max} = \frac{\gamma_{SE}}{\gamma_{SE} + \Gamma_R} = 0.70. \quad (11)$$

Realistically, the Rb polarization is $\sim$70% in the pumping chamber, which reduces the actual ^{3}He polarization to about 40–50%.

5.3.2. Target cells

The construction and filling of the target cells require great care in order to achieve $1/\Gamma_{cell}$ of 40–60 h. Cells are constructed from aluminosilicate glass, either Corning 1720[25] or, more recently, GE 180.[26] The cells are filled to a pressure of about 10 atm ^{3}He (0.69 MPa) at room temperature. The length of the cell is either 40 or 25 cm, and the diameter is 1.9 cm. The end windows are approximately 120 μm thick and the side wall is approximately 1 mm thick.

5.3.3. The optics system

As mentioned above, approximately 50 W of usable light at 795 nm is required. Light that can be readily absorbed by the Rb admixture, is considered usable. While the absorption line of Rb has a full width of only several hundred GHz at the operational high pressure of ^{3}He, a significant amount of light that is not within the absorption linewidth is still absorbed because the high Rb number density used ($\sim 4 \times 10^{14}$ atoms/cm^3) is optically quite thick.

Three 30 W diode lasers[27] are used for the optical pumping in each direction. Seven laser beamlines are used for the polarized ^{3}He target: three for longitudinal (with the nuclear spin oriented along the electron beam direction), three for transverse pumping and one as a spare. The beam of laser light coming out of the diode laser is largely unpolarized. A polarizing beam splitter makes it linearly polarized, followed by a quarter-wave plate that produces circularly polarized light. The helicity direction of the circularly polarized laser light can be reversed by a remotely controlled insertable half-wave plate. When the helicity is reversed, the holding field direction is changed accordingly.

5.3.4. Polarimetry

The target polarization is measured by two means: with the Nuclear Magnetic Resonance (NMR) technique of adiabatic fast passage (AFP) [61], in which the signals are calibrated by comparing the ^{3}He NMR signals with those of water, and by measuring the frequency shifts that the polarized ^{3}He nuclei cause on the electron paramagnetic resonance (EPR) lines of Rb atoms. Both methods were used in the first two experiments. After careful analyses, each method achieved a precision of 4% with good agreement between the two methods.

These polarimetry methods were cross-checked by measuring the asymmetry in elastic scattering off ^{3}He, because the ratio of the measured to the calculated asymmetry (from the world data set on elastic form factors) is proportional to the product of the beam and target polarization. The elastic asymmetry was found to be in good agreement with the results of the NMR and EPR polarimetry.

5.3.5. Apparatus overview

The target is in an enclosure filled with helium. Helium cooling jets on the target windows prevent the electron beam from overheating the target cell. The main components of the target include two pairs of large Helmholtz coils (one oriented parallel to the beam direction, the other

[25] Corning Inc., One Riverfront Plaza, Corning, NY 14831, USA, www.corning.com.

[26] General Electric Components Marketing and Sales Operation, 1975 Noble Road, Nela Park, Cleveland, OH 44112, USA, www.ge.com.

[27] FAP-I system, Coherent Inc., 5100 Patrick Henry Drive, Santa Clara, CA 95054, USA, www.cohr.com.

perpendicular) that are used to produce a static magnetic field of about 2.5 mT at an arbitrary angle in the horizontal plane. In addition to establishing the quantization axis for the target, the coils also suppress relaxation from magnetic field inhomogeneities.

The NMR components in the target include a set of RF drive coils, a separate set of pick-up coils, and appropriate electronics. The apparatus necessary for doing EPR polarimetry includes a small probe (housing a drive coil and a photodiode) and associated electronics. The polarimetry electronics is controlled by a PC with LabView,[28] which communicates with EPICS.

A target ladder contains, in addition to the polarized ^{3}He cell, a reference cell, a seven-foil ^{12}C target and a BeO target. The reference cell is connected to a gas-handling system and can be filled with different target gases (^{3}He, ^{4}He, N_2) at pressures ranging from 0 to 0.69 MPa. The seven-foil ^{12}C target is used to study the spectrometer acceptance. The target ladder can be moved into each target position (including an empty target) and to the pick-up coil position.

The controls for the target motion, the laser, the oven and the heater and the read-out of the temperature and pressure are all handled with EPICS. Further details on the polarized ^{3}He target can be found in Ref. [62].

5.4. The waterfall target system

The waterfall target system provides a target for experiments on ^{16}O. Using a waterfall for oxygen experiments has many advantages. Pure oxygen is difficult to handle, as it is highly reactive. The use of other oxygen compounds requires additional measurements to subtract the non-oxygen background, whereas the hydrogen in water can be used for calibration purposes. The technique of using continuously flowing water as an electron scattering target was first developed by Voegler and Friedrich [63], and later refined by Garibaldi et al. [64].

Water forced through slits forms one or more flat rectangular films which are stable as a result of surface tension and adherence to stainless steel poles. Each waterfall foil is produced in a cell mounted in the standard scattering chamber. The water, continuously pumped from a reservoir, goes through a heat exchanger into the target zone and then back into the reservoir. All parts in contact with the water are made of stainless steel. Once the target is formed, the thickness increases with the pump speed up to a maximum value. A gear pump, magnetically coupled to a DC motor, is used to produce a stable film. The target thickness stability is monitored by continuously measuring the pump speed and the flow rate. A cooler can be used to keep the water at a constant temperature.

A three-waterfall offset configuration was chosen for the commissioning of the HRS spectrometers and for two ^{16}O experiments [65,66], with each waterfall nominally 125 mg/cm^2 thick, and oriented at 30° to the incident beam. The three foils are identical, 12 mm wide, and guided by poles which are 2 mm × 2 mm with a machining tolerance of less than 0.15 mm. This configuration is superior to a single waterfall three times thicker, because the energy loss in each waterfall is reduced. Furthermore, requiring a consistent reaction vertex reduces the number of accidental coincidences, and allows a partial correction for energy loss. Care is taken to optimize the foil configuration with respect to the spectrometer acceptance and ejectile trajectory, so that the scattered particles do not go through a second water foil for any of the kinematics settings of the experiment. In order to exploit the availability of three separate films, it must be possible to track the scattered particles back to their target coordinates. The precise knowledge of the spectrometer matrix elements enables such a reconstruction. This is illustrated in Fig. 24, where the spectrum of scattered electrons is shown as a function of the coordinate perpendicular to the optical axis of the spectrometer.

The target is designed to stay at a fixed angular position: the waterfall target container is a box 630 × 68 × 8 mm^3. Because it is intended to employ beam currents exceeding 50 μA, care must be taken in choosing the window material because of the risk of melting. The entrance and exit windows are circular (30 mm in diameter) and

[28] National Instruments, sine.ni.com.

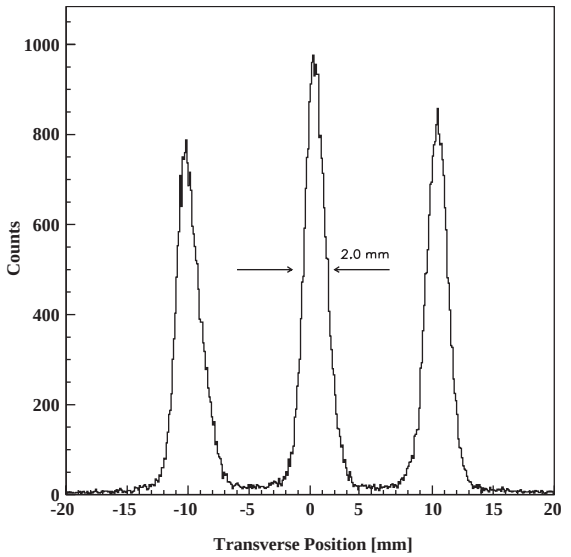

Fig. 24. The position of the three waterfall foils, reconstructed from the focal plane detector information.

made of Be (75 μm thick). Because Be is highly toxic, it has been plated with 13 μm of Ni and a monolayer of Au (which also serves to improve heat conductivity). The lateral windows, which the scattered electrons and knocked out protons must traverse, are made of stainless steel, 25 μm thick. Under the cell a target frame holds up to five solid targets. A target position can be selected remotely by a mechanical system driven by stepping motors and controlled by absolute encoders whose precision is 0.1 mm and 0.1°.

The waterfall target system has further been used for experiments E00-102 [67] and E94-107 [68]. Because the kinematics of all experiments were quasi-elastic, the H(e, e′) reaction served as a continuous luminosity monitor, while the H(e, e′p) reaction was used to determine the $\vec{q}$ direction precisely. Details of the system can be found in Ref. [69].

6. Control systems

A distributed system based on the application framework of the Experimental Physics and Industrial Control System (EPICS) (see footnote 6) is used to monitor and control various elements of the Hall A instrumentation. EPICS is also used at JLab to monitor and control both the Continuous Electron Beam Accelerator as well as the Free Electron Accelerator. The basic components of the system are:

- Operator Interfaces (OPI): UNIX based workstations able to run various EPICS tools like the Motiff Editor and Display Manager (MEDM) for display and control,
- Input/Output Controllers (IOCs): VME crates containing a computer, various Input/Output (I/O) modules (i.e. Analog to Digital Converters) as well as interfaces to other I/O buses like RS-232 (serial) or the General Purpose Instrumentation Bus (GPIB),
- Local Area Network (LAN): the communication path between the IOCs and the OPIs as well as between the IOCs.

EPICS has several interrelated characteristics that make it well suited for geographically extended control systems of medium to large size and complexity [70]:

- The use of industry standards like ethernet and TCP/IP allows a quick implementation of geographically distributed systems with the IOCs near the end devices. Depending on the extent of the system, substantial savings are obtained from shorter cable routing and not having to use signal conditioners. The number of OPIs and IOCs supported by EPICS is arbitrary and is limited only by the available network bandwidth.
- EPICS signals are uniquely identified within a network by arbitrarily assigned names instead of the network name/address of the OPI/IOC in which they reside. This allows, for example, redistribution of signals from a saturated IOC to other IOCs without having to change any other part of the system including other OPIs/IOCs making use of those signals. A similar situation applies to applications running in the OPIs.
- Event-driven software components are used as much as possible in EPICS to minimize response times and optimize the use of

resources. Two levels of event-driven software are implemented: (a) hardware interrupts are used to communicate between processors and their I/O modules and, (b) signal handlers can be triggered when the value of another signal handler changes. Tests (see footnote 6) indicate that a Motorola 68040 processor at 33 MHz (a low-end processor by today's standards), can process about 6000 signals/s including network access.

- As the complexity of a control system grows, software tools are required to create, maintain, interact and monitor the integrity of the system. EPICS provides several tools (see footnote 6) to aid with these tasks. Besides the MEDM tool mentioned earlier, some other tools are:
  - Alarm Handler (ALH): used to notify the operators when either communication with a given IOC has been lost or a monitored signal has exceeded a set threshold.
  - Backup and Restore Tool (BURT): allows rapid restoration of each IOC to a previously known working state. It can be used, for example, to restore a corrupted IOC to the settings before the problem occurred or an entire accelerator to the settings of one year ago.
  - Channel Archiver: maintains a history of selected signals.
  - Graphical Database Configuration Tool (GDCT): used to create the signal handlers which reside in an IOC and their interrelation.

The standard Hall A IOC configuration consists of VME based Motorola MVME162 [71] single-board computers executing the real-time operating system VxWorks [72]. The EPICS application executes on top of the VxWorks operating system. At the core of each IOC a memory-resident database describes each of the signals to be monitored and controlled by the IOC. Each database entry consists of a C language structure referred to as a record. EPICS has many pre-defined record templates (i.e., Analog Input or Analog Output) and new ones can be added. Each record template has a fixed number of variables. Some of these variables are common to all the record templates (i.e., a variable to hold the name assigned to a given instantiation of a record template) while others are specific to a given record template. Among the common variables, one holds the processing method to be used by a database record. Several options are available:

- Periodic. The record is processed at a set frequency (i.e., 0.5 Hz).
- Software Event. The record will be processed if its event number matches the event number posted by some other software component in the IOC.
- I/O Event. The record will be processed when an external interrupt occurs.
- Passive. The record is processed as a consequence of either external changes to the record (i.e., a new value was input by an operator) or processing of linked records.

Access (i.e. search, write and read) to the variables of each database record is through EPICS provided database manipulation functions. A detailed description of the predefined EPICS record templates, the variables that each record has, interfacing between the database records and the low-level hardware drivers as well as the routines for database access can be found in Ref. [13].

At present, there are 18 IOCs permanently located inside Hall A and a few that move in or out of the hall depending on the experimental setup. Some of the IOCs are dedicated to a specific purpose while others handle all signals to/from a region of the hall regardless of their specific purpose. Examples of specific purpose IOCs are those that handle the distribution of cryogenic fluids (helium and nitrogen) for the superconducting magnets, cryogenic targets and beam current monitoring. Examples of region-allocated IOCs are those located in the detector hut of each spectrometer or those which handle the basic infrastructure of each spectrometer (i.e., magnet power supplies, magnet power lead cooling, collimators and vacuum). The number of records being handled by the IOCs is estimated to be several thousand.

To minimize radiation effects on the IOCs (i.e. memory corruption), the IOCs are located either inside shielded enclosures like the detector hut or in the shadow cast (i.e., for gammas although not

neutrons) by thick objects such as the dipole of each spectrometer. It would have been desirable to have every piece of electronics (including the IOCs) well shielded from radiation but the limited space in the detector huts and the large angular range of both spectrometers do not allow this option. As much as possible of the critical electronics (i.e. systems that must operate for the hall to take data) was placed inside shielded enclosures. Examples are the IOCs that control the basic spectrometer infrastructure and some of the magnet power supplies' internal controllers. Systems which are either not used continuously during an experiment (i.e., spectrometer motion) or are less susceptible to radiation have been left more exposed to radiation. Remote reset lines allow rebooting any IOC which shows signs of failure or data corruption. Downtime due to radiation damage or corruption of electronics has been minimal.

7. Data acquisition

The data-acquisition (DAQ) systems in Hall A use CODA (CEBAF On-line Data Acquisition System) [73] developed by the JLab data-acquisition group. CODA is a toolkit of distributed-software components from which data-acquisition systems of varying degrees of complexity can be built. Supported hardware elements are mainly commercially available electronics, including front-end Fastbus and VME digitization devices (ADCs, TDCs, scalers), the Struck Fastbus Interface (which provides a VME interface to Fastbus), single-board VME computers, 100BaseT Ethernet networks, Unix or Linux workstations, and a mass storage tape silo (MSS)[29] for long-term data storage. The commercial software elements are the VxWorks operating system (see footnote 14) which runs on the VME computers, and either SunOS[30] or Linux[31] on the workstations. Custom hardware elements made at JLab include the trigger supervisor [74] which synchronizes the read-out of the front-end crates and handles the dead-time logic of the system, as well as interface cards for the Fastbus and VME crates which facilitate communication between the trigger supervisor and the front-end crates. The most important custom software components of CODA are the read-out controller (ROC) which runs on the front-end crates, the event builder (EB) and event recorder (ER) which run on a Unix or Linux workstation, the event-transfer (ET) system which allows distributed access to the data on-line or insertion of data from user processes, and finally the RunControl process, from which users can select different experimental configurations, start and stop runs, as well as reset and monitor CODA components. Because of the modular nature of CODA and its emphasis on commercially available components, data-acquisition systems can be built and reconfigured rapidly.

For each event, which corresponds to a trigger accepted by the trigger supervisor, data are gathered from the front-end boards by the ROC component, which buffers the data in memory and sends these buffers via the network to the EB running on a workstation. The EB builds events from fragments sent by the various ROCs and passes them to the ER which writes data to a local disk. The data are subsequently written to tapes in the MSS and erased from disk typically after one day. Using the ET system, various additional pieces of data are inserted into the data stream every few seconds from the control system, scalers, or text files of information. In addition, the ET system is used by analysis clients to obtain a random sample of data in real-time anywhere on the network.

The performance of the spectrometer DAQ system has been modeled by a mathematical expression of Poisson probability that relates the dead time to the trigger rate. The only parameters of this model are the front-end conversion times of the Fastbus modules, the size of the buffer in Fastbus, and the read-out times of the Fastbus and VME crates (note that most of the VME modules do not support buffering). No other parameters of

[29] Manufactured by StorageTek Inc., Louisville, CO, USA, www.storagetek.com.

[30] Developed by SUN Microsystem, www.sun.com.

[31] LINUX Software distributed by Red Hat Software Inc., Durham, NC, USA, www.redhat.com.

the system, neither of the network nor of the workstation performance, are relevant under normal running conditions. This model gives confidence that the system is well understood and that the performance has been optimized. Typically, a 2 kHz trigger rate results in a 20% dead time.

8. Data analysis

The Hall A physics data analysis model is straightforward. Raw data from the data acquisition (DAQ) are decoded and analyzed by an event-processing program. The event processor creates data summary files that contain raw and computed data, typically in ntuple and histogram format. Diagnostic information as well as final physics results are then extracted from the summary files with the help of interactive analysis tools such as PAW [75] and ROOT [76]. This general scheme applies to both on-line and off-line analysis.

For on-line analysis, experimenters have the option of analyzing either raw data stored in files on local disks of the DAQ computers or a random sample of the raw data stream that is distributed via network in real time. Network distribution is provided by the ET component of the CODA [95] DAQ system.

Raw data files are typically processed shortly after acquisition (quasi-offline analysis). This method is particularly suitable if the on-line data rate is relatively low (typically below 1 k events/s) or while no data are being taken. At higher rates, simultaneous read and write access to the raw data storage may increase the DAQ computer deadtime. Such deadtime problems can be avoided by using the ET system; the main disadvantage of this system is that only a sample of the data, instead of the entire data set, can be analyzed.

For off-line analysis, the raw data files are qfirst retrieved from the JLab Mass Storage System (“tape silo”) to staging disks, from where they can be processed either interactively or as part of a batch job. For batch processing, the JLab Computer Center maintains a large PC farm, which at the time of this writing consists of 370 CPUs delivering approximately 11,500 SPECint95 [77]. The farm is shared among the various user groups from all three experimental halls performing data analysis. Interactive analysis is usually carried out on individual desktop computers or small PC clusters owned by individual groups. To date, virtually all farm and desktop systems run Linux.

8.1. General features

For the past several years, Hall A has been using the FORTRAN-based program ESPACE (Event Scanning Program for Hall A Collaboration Experiments) [78] as the standard physics event-processing software. ESPACE was originally developed at Mainz and improved at MIT before being introduced in Hall A in 1995. It is written in FORTRAN 77 with the addition of many VMS-style (DEC Fortran) extensions such as structures and pointers. Common operations such as histogramming, graphics, and macro processing are implemented using various CERNLIB [79] packages.

ESPACE’s capabilities include:

- reading, decoding, and scaling (calibrating) raw event data,
- reconstruction of wire chamber tracks, computation of spectrometer focal-plane coordinates and target quantities,
- computation of basic physics quantities (e.g., angles, four-vectors, kinematics),
- dynamic definition of conditional tests (cuts) and selection of event data based on these tests,
- dynamic definition of histograms and ntuples and output of these in HBOOK [80] format,
- fitting of analysis parameters (e.g., timing and position offsets, spectrometer reconstruction matrix elements) to experimental data (“optimization”),
- display of single events in terms of detector hits in a graphics window,

- program control and analysis steering via the Kit for a User Interface Package (KUIP) [81].

A dynamic definition of tests and histograms is implemented by the COOLHANDS package [82], which is accessible directly from KUIP.

ESPACE has been used to date by almost all Hall A experiments for production data analysis. Its main advantages are the fact that it is relatively well debugged and has been adapted to the specific Hall A requirements. Its track reconstruction algorithm is sophisticated and provides high efficiency and resolution. The typical analysis speed is 100–200 events/s on a 500 MHz Linux PC.

In the following, a detailed description of the tracking and reconstruction algorithm used in ESPACE is given.

8.2. Tracking and reconstruction algorithm overview

Tracking information is obtained from the two vertical drift chambers (VDCs) in each spectrometer. The layout of the VDCs is illustrated in Fig. 9. An important advantage of the two-chamber design is that it provides a long lever arm for the measurement of track angles, resulting in high angular tracking resolution. Global track angles are determined from the two track cross-over positions measured in the two VDCs. The cross-over positions can be reconstructed with very high precision and are insensitive to the details of the reconstruction algorithm. Knowledge of the *local* track angles in each wire plane is not necessary.

The tracking analysis can be divided roughly into the following steps:

(1) hit selection,
(2) cluster identification,
(3) TDC corrections,
(4) local cluster fitting,
(5) If multiple clusters are found in any plane:
  (a) path analysis,
  (b) global cluster fitting,
  (c) path selection,
  (d) "Golden Track" selection.
(6) Focal-plane coordinate transformations.
(7) Reconstruction of target coordinates.

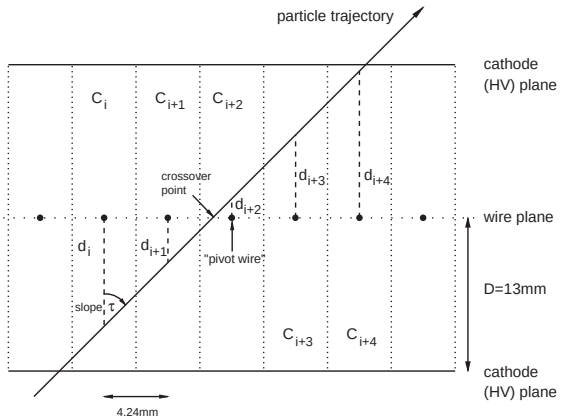

Fig. 25. A typical cluster of hits in a VDC plane. C_i denotes the ith wire cell, and d_i represents the perpendicular (effective) drift distance within that cell. The ith cell is defined as the region within which ions drift to the ith wire. By symmetry, the cell boundaries lie halfway between wires. The wire spacing is 4.24 mm. The separation between cathode high-voltage and wire planes is approximately 13 mm. The HV planes are held at a potential of approximately -4 kV, while the wires are effectively grounded.

We examine each step more closely in the following.

8.3. Hit detection and selection, and cluster identification

Fig. 25 illustrates the passage of a charged particle through a VDC plane. Along its way, the particle ionizes the gas in the chamber. Ions and electrons generated in this process drift with nearly constant velocity along the lines of the electric field between the wires, which are grounded, and the cathode planes, which are held at a negative potential of about -4 kV. As the field intensifies in the region close to the wires, drifting electrons accelerate and cause further ionizations, resulting in an avalanche which induces an electrical signal (hit) on the wire. The signals are preamplified and sent to TDCs.

The TDCs are capable of recording multiple hits per event and are operated in the common-stop mode. If multiple hits occur on a wire, the first hit corresponds to the largest TDC value. ESPACE uses only these first hits for further analysis, and all subsequent hits on a given channel are ignored.

This approach is reasonable because multiple hits per wire are often associated with electronic ringing or track-induced noise, where only the leading edge of the signal is physically meaningful. A typical spectrum of the TDC values of the first hits is shown in the lower left panel of Fig. 10.

To eliminate noise further, hits that do not satisfy the condition $-0.5D \leqslant t \times \eta \leqslant 1.5D$ are cut from the input data. Here, D is the distance between the wire and the cathode planes (13.0 mm), t the measured drift time, and η the average electron drift velocity in the chamber (50 μm/ns).

Once hits have been selected, clusters are identified. Clusters consist of hits with consecutive wire numbers. To allow for inefficiencies, clusters are allowed to have gaps of one wire without a hit. By design, good tracks cross the VDCs at an angle of approximately 45°, corresponding to an angle of 55° with respect to the wire planes (cf., Eq. (18)). Thus, there are typically four to six hits in a cluster.

8.4. TDC corrections

In principle, tracks can be reconstructed using only the cluster center coordinates, which can be obtained from the known wire locations; however, the spatial resolution per plane available in this way is of order of the wire separation (4.2 mm), which is not sufficient to meet the precision requirements of the Hall A spectrometers. Better resolution can be obtained by analyzing the TDC timing information. The TDC data allow extraction of the projected drift distances d_i within each wire cell C_i (see Fig. 25). Once the distances d_i are known, the cross-over point of the track in the wire plane can be determined with very high precision by a linear fit of drift distances vs. wire positions. The typical per-cluster position resolution obtained with the Hall A VDCs using this method is 225 μm FWHM [18].

The TDCs directly measure the time between ionization and the arrival of the signal at the wire (the "drift time"). The extraction of precise drift distances d_i from the measured drift times requires a more detailed analysis. The raw TDC data must be corrected for a number of effects:

(1) the time of flight between the cluster centroid and the first scintillator plane (S1);
(2) the dependence of the trigger scintillator timing on the amplitude of the scintillator signal ("timewalk"); and
(3) the non-linear relationship between drift time and drift distance.

While the first two corrections are relatively minor, the third one is important. The relationship between drift time and absolute drift distance is non-linear because of the non-uniform electric field within the cells; in particular, the mean drift velocity increases near the wires. The dependence of distance on time can be parameterized either analytically based on calculations or empirically based on data [18,83].

Three different parameterizations are implemented in ESPACE to linearize the drift times:

(1) a fourth-order polynomial with fitted coefficients [83];
(2) a third-order polynomial with coefficients obtained from a GARFIELD [83,84] simulation; and
(3) a two-dimensional lookup table generated from calibration data [18].

In practice, the most stable results are usually obtained with the first method.

Internally, ESPACE does not compute drift distances directly, but rather equivalent linearized drift times. Multiplication of these times with the average drift velocity η yields drift distances. This approach allows a constant timing offset to be fitted along with the track parameters. This is important in the multi-cluster analysis (see Section 8.6).

The precision of the TDC corrections is not critically important for the precision of the final tracking results. Because of the symmetry of the cluster fit geometry, imprecise TDC data increase predominantly the error in the local track *angles*. The fitted cross-over positions are relatively insensitive to details of the corrections, with a highly symmetric cluster being the least sensitive. Eventually, only the local cross-over points, not

the angles, are used to compute the track parameters (see Eqs. (20) and (21)).

8.5. Local cluster fitting

After determination of the TDC corrections, track positions and angles are extracted from the cluster data.

If only one cluster is found per wire plane, a standard linear fit is performed on each cluster in each wire plane, and the analysis continues with the fitted local positions and slopes. Specifically, the fit is performed on the variables

$$x_i = S_i \cdot \eta(t_{\mathrm{off},i} - t_i + t_{\mathrm{corr},i}) \tag{12}$$

$$y_i = w_i - w_0 \tag{13}$$

where η is the average electron drift velocity, $t_{\mathrm{off},i}$ the TDC value for zero drift time (the "TDC offset") for the ith wire, t_i the measured TDC value for that wire, and $t_{\mathrm{corr},i}$ the sum of the TDC corrections explained above. The constants w_i represent the position of the ith wire. The relevant geometry is shown in Fig. 25. The quantity $S_i = \pm 1$ is the sign of the ith drift distance. The sign S_i is ambiguous because the TDC data contain no information as to whether a track passed below or above a wire and is determined in a separate step as explained below. The result of the fit are the intercept u (v for V planes), slope τ_u (τ_v), their respective uncertainties, and χ^2. Note that, with these definitions, the slope τ vanishes when the track is perpendicular to the wires.

To resolve the ambiguity in the sign of the calculated drift distances, one observes that good tracks traverse the chamber at an angle of approximately 55° with respect to the u (v) axis. Assuming a given track satisfies this criterion, all hits with smaller u (v) coordinates than the cross-over point of the track in the wire plane can be assigned negative drift distances. The cross-over point can be taken to coincide with the wire that has the smallest drift distance ("pivot wire"). An ambiguity remains about the sign of the drift distance to be assigned to the pivot wire. It can be resolved by trial-and-error: two fits are performed, one with a positive and one with a negative value of the drift time of the pivot wire, and the fit with the smaller χ^2 is assumed to be correct.

The above method for resolving the sign ambiguity and determining the track parameters through a fit only works for clusters with three or more hits. For clusters with only two hits, it is usually possible to guess the signs of the two distances by requiring that the track slope be close to 55°. Thus slope and intercept can be estimated, albeit with reduced precision and confidence. This procedure slightly improves the tracking efficiency at the expense of a lower resolution for some tracks. "Clusters" consisting of only one hit do not yield sufficient information and are discarded.

At this point in the analysis, ESPACE distinguishes two cases:

- Exactly one cluster per plane. This is a "single-cluster event". The analysis continues as described in Section 8.7.
- More than one cluster in at least one plane. This is considered a "multi-cluster event", even if only a single plane has multiple clusters. In this case, the analysis continues as described in the next section.

8.6. Multi-cluster analysis

Multiple clusters in a wire plane may occur for several reasons:

- Noise, which may originate, for example, from the electronics, cosmics, or radiation background. True noise clusters usually do not give reasonable fit results and thus are easy to remove. Cosmics coincident with an actual track are normally very rare due to the low cosmics rate. Cosmics and certain background noise may lead to valid tracks through the chamber, but can usually be eliminated easily because of unreasonable angles, reversed scintillator timing, and, eventually, failure to reconstruct to the target.
- Actual multiple tracks from the target. These may occur for essentially two reasons: (a) several tracks emitted from the same interaction in the target fall within the acceptance of the spectrometer; and (b) accidental coincidences of tracks from two separate interactions occur

within the VDC timing window. The former case is rare because the Hall A spectrometers do not have a sufficiently large acceptance to be able to cover much of the phase space for multiparticle events. The latter case may occur rather frequently at sufficiently high singles rates, and thus it is the most likely cause of multi-track events. Usually, all tracks in true multi-track events can be reconstructed.

- Spurious tracks caused by delta rays, which are produced before or in the wire chamber by actual tracks. Such tracks often have unreasonable angles and/or do not make clusters in all wire planes (e.g., if they are generated inside the chamber); however, as they may occur close to actual tracks, they may cause overlapping clusters and thus corrupt valid tracking information. This may be a difficult situation to analyze, and actual tracks may not always be recoverable. An upper limit on the probability that spurious tracks occur in the chamber that disturb the regular tracking data is given by the abundance of clusters with high hit multiplicity. Typically, about 3–4% of events in each spectrometer are found to have one or more clusters with eight or more hits. Such clusters cannot occur due to normal tracks alone and contain either spurious hits or are entirely due to tracks not originating from the target.

If multiple clusters occur in any plane, the association between clusters and tracks may become ambiguous. To determine the most probable track(s) through the chamber, an approach well known in wire chamber analysis is taken within ESPACE. All possible combinations of clusters from the four VDC planes are identified (each combination containing exactly one cluster from each plane), and each such combination is considered a possible path of the track through the chambers. A fit is then performed for each path, and the paths are ordered by the fit's total χ^2. The path(s) with the smallest χ^2 represent(s) the best reconstructed track(s).

In the following sections these steps are described in detail. As this algorithm is relatively involved and not guaranteed to yield improved tracking results, it is sometimes considered safer to disregard any events with multiple clusters per wire plane altogether at the expense of tracking efficiency and to consider only unambiguous single-cluster events.

8.6.1. Path analysis

To identify paths through the chamber, ESPACE considers the wire planes in the order U1, U2, V1, and V2 (see Fig. 9). This sequence is preferable over the actual physical sequence because hits from like wire planes (U or V) can be fitted together.

For every cluster in plane U1, all combinations ("links") with clusters in plane U2 are considered. The cluster in U1 is considered the "start point", and the cluster in U2, the "end point" of the link. There are $n_{u1}n_{u2}$ such links, where n_{u1} and n_{u2} are the numbers of clusters in U1 and U2, respectively. For each link, a fit is performed on the combined hits (typically $2 \times 5 = 10$) of the clusters from both planes, U1 and U2. The fitting procedure used is described in the next section in more detail. The resulting χ^2, cross-over position, timing offset t_0, and track slope are stored with the link. This procedure is repeated identically for the combination of planes V1 and V2. For the combination U1 and V1, it is not possible to perform a fit since the wire directions of the planes are orthogonal. Thus, only the possible links between these planes are stored.

Next, a table is built of all connecting combinations of links. Two links connect if the end point of a link in one plane is the start point of a link in another plane. Thus, each combination contains exactly three links, one between each pair of wire planes in the sequence U1–U2, U2–V1, and V1–V2. There are $n_{u1}n_{u2}n_{v1}n_{v2}$ such combinations. Each is a possible path for the track.

8.6.2. Global cluster fitting

In a multi-track situation or in the presence of noise, tracks other than the one that generated the event trigger will, in general, occur at times other than the trigger; a fit to the drift times must, therefore, allow for a timing offset, called t_0. Clusters belonging to the "Golden Track" (the track that generated the trigger) will have $t_0 \approx 0$, while clusters belonging to other tracks will, in

general, have a non-zero fitted time offset. To accommodate t_0, ESPACE uses a three-parameter fit in the multi-track analysis. The fit routine used is derived from the `curfit` algorithm of Bevington [85]. This is an iterative algorithm which is computationally relatively expensive.

As in the single-track case, the ambiguity of the pivot-wire drift time must be resolved. This is again done by trial-and-error; however, since two clusters from two different wire planes are involved in the multi-cluster fit, *four* fits are performed on the same data, corresponding to the four possible sign combinations of the two pivot wires. The result with the smallest χ^2 is chosen. (The number of fits is the same as in the case of single clusters, of course, although the single-cluster fit algorithm is simpler and fewer data are processed with each fit.)

The computational requirements of this algorithm are relatively high. For instance, if two real tracks are present, generally there will be two clusters in each plane, and so $2^4 = 16$ paths to consider. Because a single path contains two pairs of wire planes (U1–U2 and V1–V2) that are fitted together, eight fits are performed for each path to resolve all ambiguities. As a result, $16 \times 8 = 128$ iterative fits must be carried out to identify two tracks.

8.6.3. Path ordering and track identification

Next in the analysis, paths are ordered according to a goodness-of-fit criterion, and the best-fit result(s) are selected. To order paths by their probability of describing a valid track, ESPACE uses the quantity

$$\chi^2_{\mathrm{tot}} = \chi^2_{u1u2} + \chi^2_{v1v2} + \left(\frac{t_{0,v1v2} - t_{0,u1u2}}{\min(\sigma(t_{0,v1v2}), \sigma(t_{0,u1u2}))} \right)^2 . \quad (14)$$

Here, χ^2_{u1u2} and χ^2_{v1v2} are the χ^2-values found in the U1–U2 and V1–V2 global cluster fits, respectively, $t_{0,u1u2}$ and $t_{0,v1v2}$ are the timing offsets obtained from these respective fits, and the $\sigma(t_0)$ are the uncertainties in those offsets. The minimum uncertainty of the two t_0 fits is used, rather than the combined uncertainty, in order to give smaller χ^2 in situations where the two t_0 fits have comparable rather than dissimilar uncertainty. Using the difference of timing offsets as a goodness-of-fit criterion between the planes U2 and V1 is the best that can be done under the circumstances. Because the U and V coordinates are orthogonal, there is no good criterion for matching U and V clusters other than their timing. This is a design limitation of the Hall A VDCs. Different chamber designs include additional wire planes oriented in a third direction that allow easier correlation between clusters in different planes.

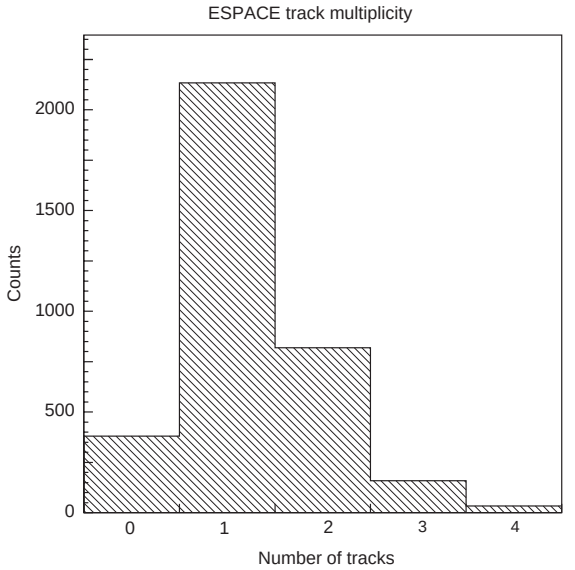

Fig. 26. Typical VDC track multiplicity determined by ESPACE in a high-rate environment (200 kHz of electron singles triggers).

Possible physical tracks are now selected from the ordered paths. This step relies on the assumption that each cluster belongs to at most one physical track, which is correct so long as clusters from different tracks do not overlap. ESPACE selects the maximum number of tracks from the available paths that do not have any clusters in common, starting from the path with smallest χ^2_{tot}. Note that this means, for example, that in order to find two valid tracks, *every* VDC plane must have at least two clusters. Even if many possible paths were found in the preceding analysis, only a small number of tracks survive at this point. A typical

histogram of the track multiplicity in a high-rate experiment is shown in Fig. 26. In general, tracking results are only considered useful for physics analysis if a single track is found. Events with multiple tracks are typically discarded (see Section 8.8). Using the single track criterion, the overall tracking efficiency varies between better than 95% at low rate and 70–80% at high rate.

8.6.4. Golden Track selection

The final step in the multi-cluster analysis is to select the Golden Track from the set of tracks determined in the previous analysis. The timing offset t_0 obtained from the global cluster fits (Section 8.6.2) can be used as a direct measure of the probability of a track to have generated the trigger. ESPACE uses the weighted average of the two timing offsets obtained, viz.

$$t_{0,av} = \frac{\frac{t_{0,u1u2}}{\sigma(t_{0,u1u2})^2} + \frac{t_{0,v1v2}}{\sigma(t_{0,v1v2})^2}}{\frac{1}{\sigma(t_{0,u1u2})^2} + \frac{1}{\sigma(t_{0,u1u2})^2}} \tag{15}$$

to select the Golden Track. The quantities t_0 and $\sigma(t_0)$ in Eq. (15) are the same as in Eq. (14). The track with the smallest $t_{0,av}$ is chosen. Further analysis continues with this track only, and all other tracks found are subsequently ignored.

8.7. Coordinate transformations and target reconstruction

In the preceding analysis, the track through the VDC has been determined in terms of wire plane coordinates, u and v. For further analysis, it is advantageous to convert the track coordinates to detector coordinates: x_{det} and y_{det}, and their corresponding angular coordinates, θ_{det} and ϕ_{det}. (By convention, θ_{det} and ϕ_{det} denote the tangents of the respective angles.) The relationship between the coordinate systems is shown in Fig. 27. The coordinate transformation can be written as

$$x_{\mathrm{det}} = \frac{u\sin\gamma - v\sin\beta}{\sin(\gamma-\beta)} \tag{16}$$

$$y_{\mathrm{det}} = \frac{u\cos\gamma - v\cos\beta}{\sin(\gamma-\beta)} \tag{17}$$

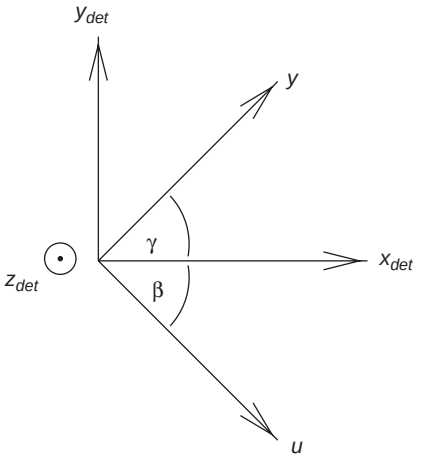

Fig. 27. Top view of the wire plane and VDC detector coordinate systems. The u and v axes are perpendicular to the wires of the U and V planes, respectively, and point in the direction of increasing wire numbers. The x-axis lies in the horizontal plane and points along the spectrometer dispersive direction (the long side of the VDC frame) such that x_{det} increases as momentum increases. z_{det} points vertically up, and y_{det} is oriented along the non-dispersive direction to form a right-handed coordinate system. The u and v-axes form angles β and γ with respect to the VDC x-axis. For the Hall A VDCs, $\gamma = 45^\circ$ and $\beta = -45^\circ$.

$$\theta_{\mathrm{det}} = \frac{\sin\gamma\tan\alpha_u - \sin\beta\tan\alpha_v}{\sin(\gamma-\beta)} \tag{18}$$

$$\phi_{\mathrm{det}} = \frac{\cos\gamma\tan\alpha_u - \cos\beta\tan\alpha_v}{\sin(\gamma-\beta)}. \tag{19}$$

Here, α_u and α_v are the global track angles in the u–v coordinate system, i.e., the angles between the z-axis and the projection of the track onto the u–z and v–z planes, respectively. In the single-cluster analysis, α_u and α_v are calculated using the fitted cross-over points u_1, u_2, v_1, and v_2 in the U1, U2, V1, and V2 planes, respectively, as follows:

$$\tan\alpha_u = \frac{u_2 - u_1}{d_u} \tag{20}$$

$$\tan\alpha_v = \frac{v_2 - v_1}{d_v} \tag{21}$$

where d_u and d_v are the separations of like planes, as illustrated in Fig. 9. In general, $\tan\alpha_u$ and $\tan\alpha_v$ will be close to the local cluster slopes τ_u and τ_v (cf., Section 8.5 and Fig. 25). In the multi-cluster analysis, α_u and α_v are determined directly in the

global fit procedure (Section 8.6.2) and are not calculated according to Eqs. (20) and (21).

The coordinates u and v in Eqs. (16) and (17) are given by

$$u = u_1 \tag{22}$$

$$v = v_1 - d_{uv1} \tan \alpha_v \tag{23}$$

where d_{uv1} is the separation between the U1 and V1 planes.

If any VDC plane has no cluster at all, attempts are made to estimate the track parameters from available local data in another plane. For instance, if the U2 cluster is missing, then the global track angle α_u can be approximated by the available local angle in U1:

$$\tan \alpha_u = \tau_{u1}. \tag{24}$$

Similar replacements are made if other clusters are missing. In this way, up to one missing u and one missing v cluster can be tolerated at the expense of reconstruction precision. This missing cluster substitution occurs only if no plane has more than one hit—it is not compatible with the multi-cluster analysis described above.

Finally, ESPACE converts the VDC coordinates to focal-plane coordinates, which are suitable as input for the target reconstruction matrix multiplication. Focal-plane coordinates as well as the target reconstruction formalism are discussed in Section 9.2.1.

8.8. Limitations

The chief shortcomings of the ESPACE software are its lack of flexibility, maintainability, and to a lesser extent its lack of speed and it heavy reliance on legacy components such as CERNLIB, KUIP, and HBOOK. The first two issues are of particular concern in view of planned detector upgrades and reconfigurations in Hall A. The addition of new detectors and the handling of multiple experimental configurations is not well supported by ESPACE and would require a significant effort to implement.

The most significant limitation of the tracking algorithm is its inability to handle overlapping clusters of hits, even though sufficient information to analyze such clusters is in principle available due to the use of multi-hit TDCs. In the present implementation, ESPACE has no provision for handling this situation. Without special processing, overlapping clusters often corrupt the tracking information. Such events are not analyzable, resulting in a tracking inefficiency. The magnitude of this inefficiency is difficult to estimate, however, because ESPACE does not provide unambiguous information as to which events were not analyzable due to overlapping clusters or due to other reasons, nor are overlapping clusters even identified. This has prompted experiments that have taken high-rate data to discard multi-cluster events altogether in the analysis. The ratio of multi-cluster events to single-cluster events is well defined, and so the inefficiency due to omitting multi-cluster events can be readily calculated.

8.9. New developments

To address many of the shortcomings of ESPACE, an effort is currently underway in Hall A to develop new analysis software using a flexible and highly maintainable object-oriented design implemented in C++ [86]. The new analyzer is based on the ROOT system [76], an object-oriented framework that has been under development at CERN since 1995 and has been adopted widely in the nuclear and particle physics community and elsewhere. The new analysis software is currently under active development and will be described in a future publication.

9. Optics commissioning of the HRSs

9.1. Introduction

The HRSs have focusing properties that are point-to-point in the dispersive direction. The optics matrix elements allow the reconstruction of the interaction vertex from the coordinates of the detected particles at the focal plane. Data obtained with a set of foil targets (which define a set of well-defined interaction points along the beam) and a sieve–slit collimator were used to determine the optical matrix elements. The Hall A

event analyzer ESPACE (Section 8.1) and a newly written C++ optimization routine [87] were used to derive optical matrix elements from these calibration data.

9.2. Acceptance

Due to the combination of a 10 cm extended target capability and a 10% momentum acceptance, the angular acceptance of the HRS devices is a complex function of momentum and target position. The acceptance of the spectrometers has been modeled by means of Monte Carlo simulations. In that modeling the raytracing program SNAKE [9] was used to trace trajectories, spanning the full acceptance and more, through the magnetic fields in each of the spectrometers. The descriptions of the magnetic fields are based on a combination of the original design parameters, survey information regarding the achieved physical locations of the magnets, and the results of the magnetic field mapping [13]. The location and direction of these trajectories are recorded at each of the critical apertures along the spectrometers. The critical apertures are those that have been identified as defining the acceptance. They are the exit of the Q_1 quadrupole, the entrance of the dipole, the exit of the dipole, and both the entrance and exit of the Q_3 quadrupole. Transfer functions from the target to each of these apertures of up to fifth order are determined using a polynomial fitting program. These transfer functions along with the knowledge of the physical size of each of the apertures are used to provide a test of whether or not any given trajectory in a Monte Carlo simulation will make it through the spectrometer. Except at extreme values of y_0 and δ comparisons of actual data with simulations have been found to agree at the 3% level or better. Updated optics models have been generated which improve the performance of the acceptance model and develop schemes for defining an acceptance through software cuts on trajectories that make optimal use of the full acceptance.

9.2.1. Approach

For each event, two angular coordinates ($\theta_{\rm det}$ and $\phi_{\rm det}$) and two spatial coordinates ($x_{\rm det}$ and $y_{\rm det}$) are measured at the focal plane detectors. The position of the particle and the tangent of the angle made by its trajectory along the dispersive direction are given by $x_{\rm det}$ and $\theta_{\rm det}$, while $y_{\rm det}$ and $\phi_{\rm det}$ give the position and tangent of the angle perpendicular to the dispersive direction. These focal plane variables are corrected for any detector offsets from the ideal central ray of the spectrometer to obtain the focal plane coordinates $x_{\rm fp}$, $\theta_{\rm fp}$, $y_{\rm fp}$, and $\phi_{\rm fp}$. A detailed description of the Hall A optics coordinate systems is given in Ref. [88]. These observables are used to calculate $\theta_{\rm tg}$, $y_{\rm tg}$, $\phi_{\rm tg}$ and δ for the particle at the target by matrix inversion of Eq. (2) which links the focal-plane coordinates to the target coordinates (in a first-order approximation).

In practice, the expansion of the focal plane coordinates is performed up to fifth order. A set of tensors Y_{jkl}, T_{jkl}, P_{jkl} and D_{jkl} links the focal-plane coordinates to target coordinates according to[32]

$$y_{\rm tg} = \sum_{j,k,l} Y_{jkl}\theta_{\rm fp}^{j} y_{\rm fp}^{k}\phi_{\rm fp}^{l}, \tag{25}$$

$$\theta_{\rm tg} = \sum_{j,k,l} T_{jkl}\theta_{\rm fp}^{j} y_{\rm fp}^{k}\phi_{\rm fp}^{l}, \tag{26}$$

$$\phi_{\rm tg} = \sum_{j,k,l} P_{jkl}\theta_{\rm fp}^{j} y_{\rm fp}^{k}\phi_{\rm fp}^{l}, \quad \text{and} \tag{27}$$

$$\delta = \sum_{j,k,l} D_{jkl}\theta_{\rm fp}^{j} y_{\rm fp}^{k}\phi_{\rm fp}^{l} \tag{28}$$

where the tensors Y_{jkl}, T_{jkl}, P_{jkl} and D_{jkl} are polynomials in $x_{\rm fp}$. For example,

$$Y_{jkl} = \sum_{i=0}^{m} C_i x_{\rm fp}^{i}. \tag{29}$$

Mid-plane symmetry of the spectrometer requires that $(k+l)$ is odd for Y_{jkl} and P_{jkl}, while $(k+l)$ is even for D_{jkl} and T_{jkl} (Fig. 28).

In practice, the basic variables $y_{\rm tg}$, $\theta_{\rm tg}$ and $\phi_{\rm tg}$ do not form a good set of variables for the optics calibration procedure. For a foil target not located at the origin of the target coordinate system $y_{\rm tg}$ varies with $\phi_{\rm tg}$. In the case of a multi-foil target, $\phi_{\rm tg}$ calculated for a given sieve–slit hole depends

[32] The superscripts denote the power of each focal plane variable.

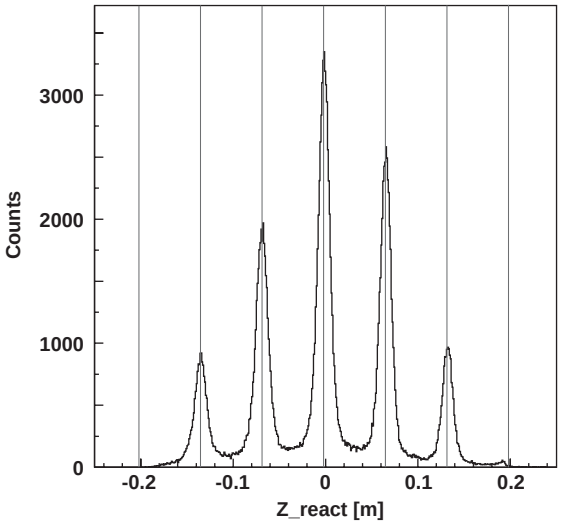

Fig. 28. Reconstructed position along the beam line (z_{react}) for 860 MeV electrons scattered from a set of ^{12}C foil targets. The lines indicate the expected positions of the foils. The spectrometer was set at 16° to the beam. The z_{react} resolution for the central foil is 1.5 cm (FWHM). Note that this corresponds to about 4 mm (FWHM) resolution in the y_{tg} direction.

on y_{tg}; furthermore, all three variables depend on the horizontal and vertical beam positions (x_{beam} and y_{beam}[33]). On the other hand, the interaction position along the beam, z_{react}, and vertical and horizontal positions at the sieve plane, x_{sieve} and y_{sieve}, are uniquely determined for a set of foil targets and a sieve–slit collimator. These three variables are calculated by combining the "basic" variables defined above using the equations (see Fig. 29):

$$z_{react} = -(y_{tg} + D)\frac{\cos(\arctan\phi_{tg})}{\sin(\theta_0 + \arctan\phi_{tg})} + x_{beam}\cot(\theta_0 + \arctan\phi_{tg}) \quad (30)$$

$$y_{sieve} = y_{tg} + L\phi_{tg} \quad (31)$$

$$x_{sieve} = x_{tg} + L\theta_{tg}. \quad (32)$$

L is the distance from Hall center to the sieve plane, while D is the horizontal displacement of the spectrometer axis from its ideal position. The spectrometer central angle is denoted by θ_0. The vertical coordinate x_{tg} is calculated using θ_{tg}, z_{react} and the vertical displacement of the spectrometer from its ideal position.

[33] Beam variables are measured in the Hall coordinate system, centered at the center of the Hall with $\hat{x}$ towards the left of the beam, $\hat{z}$ along the beam direction and $\hat{y}$ vertically up.

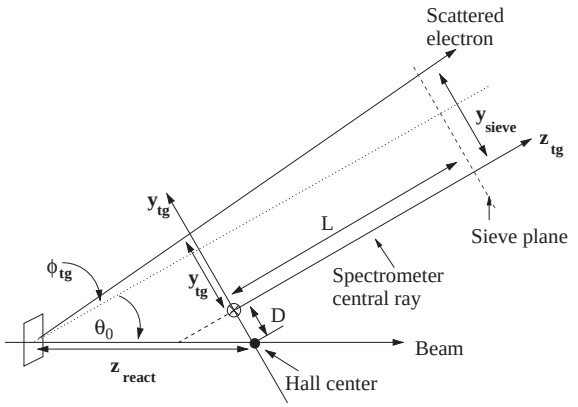

Fig. 29. Coordinates for electrons scattering from a thin foil target. **L** is the distance from Hall center to the sieve plane, while **D** is the horizontal displacement of the spectrometer axis from its ideal position. The spectrometer central angle is denoted by θ_0. Note that x_{tg} and x_{sieve} are vertically down (into the page)

The optics tensor coefficients are determined from a χ^2 minimization procedure in which the events are reconstructed as close as possible to the known position of the corresponding foil target (in the case of z_{react}) or the sieve–slit hole (in the case of y_{sieve} and x_{sieve}). The quality of the track reconstruction procedure is illustrated in Figs. 7 and 28.

9.2.2. Optics commissioning results

The following results were obtained from elastic scattering data taken at $E_0 = 845$ MeV on a thin ^{12}C target. An example of a momentum spectrum used in this analysis is shown in Fig. 30. All quantities have been measured at the target.

- Relative angular-reconstruction accuracy
  - in-plane (transverse): ±0.2 mrad;
  - out-of-plane (dispersive): ±0.6 mrad.
- Angular Resolution (FWHM)
  - in-plane (transverse): 2.0 (2.6) mrad;
  - out-of-plane (dispersive): 6.0 (4.0) mrad.
- Momentum Resolution (FWHM): 2.5 (2.6) × 10^{-4}

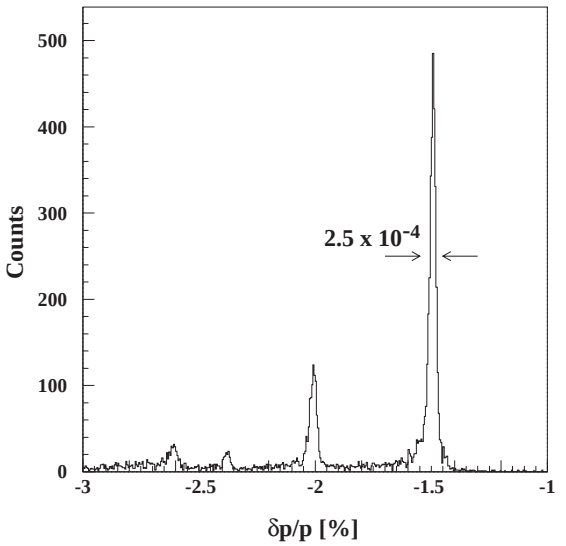

Fig. 30. The momentum of the scattered electron in the $^{12}C(e,e')$ reaction, indicating a FWHM of 2.5×10^{-4} at $\delta p/p = -1.5\%$. The beam energy was 845 MeV, the scattering angle 16°. The observed momentum resolution is consistent with the design value of 1×10^{-4} when multiple scattering from the windows of the scattering chamber and of the HRS entrance is taken into account.

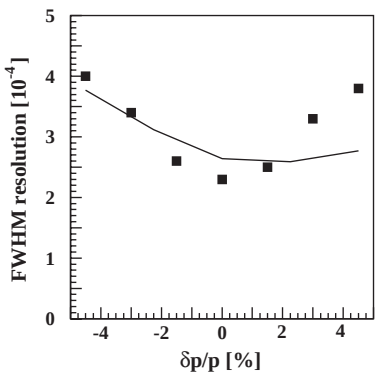

Fig. 31. The FWHM momentum resolution $\delta p/p$ measured in the reaction $^{12}C(e,e')$ as a function of the momentum of the scattered electron. The curve represents the result of a simulation, taking into account the optical properties of the HRS device and multiple scattering effects.

- Relative transverse position reconstruction accuracy: ± 0.3 mm.
- Transverse position resolution (FWHM): 4.0 (3.1) mm.

Values in parentheses are an estimate of the resolution values based on the design optics and multiple scattering in the various windows and detectors. The momentum resolution quoted above is for the center of the focal plane. Away from the center, the resolution increases (see Fig. 31). This is because the actual focal plane of the spectrometer does not coincide with the ideal focal plane used for measurements. As a result, the first-order θ-dependent term becomes increasingly large as δ moves away from 0, making the momentum determination increasingly sensitive to the measurement of the trajectory direction and, hence, more sensitive to multiple scattering.

9.3. Scattering angle determination

The electron scattering angle, θ_{scat}, is calculated by combining ϕ_{tg} and θ_{tg} (measured relative to the central ray of the spectrometer) and the spectrometer central angle θ_0 between the beamline and the spectrometer nominal central ray:

$$\theta_{scat} = \arccos \times \left(\frac{\cos(\theta_0) - \phi_{tg} \sin(\theta_0)}{\sqrt{1 + \theta_{tg}^2 + \phi_{tg}^2}} \right) \quad (33)$$

Thus, the accuracy of the scattering angle determination depends on the accuracy of ϕ_{tg} and θ_{tg} relative to the central ray of the spectrometer. The accuracies quoted above are the relative accuracies of ϕ_{tg} and θ_{tg} with respect to the central sieve–slit hole. This makes the determination of ϕ_{tg} and θ_{tg} angles for the central sieve–slit hole crucial for the determination of the scattering angle. The values of ϕ_{tg} and θ_{tg} for the central sieve–slit hole are calibrated by using electron scattering from a thin ^{12}C target located close to the Hall A center. The two angles for the electrons passing through the central hole are calculated from the following survey information:

- the target position
- the spectrometer central angle
- the displacement of the spectrometer nominal central ray from the Hall center

- the position of the sieve–slit center with respect to the nominal central ray
- the position of the beam position monitors with respect to the ideal beam line.

Each of these measurements has approximately a 0.5 mm systematic uncertainty. With the distance from the target to the sieve collimator being about 1.18 m, the total contribution of these measurements (added in quadrature with relevant weights) to the scattering-angle accuracy is about 0.6 mrad. However, once the central sieve–slit hole angles are calibrated relative to the nominal central ray, this uncertainty will remain a constant systematic offset to the scattering angle.

An alternate method utilizes the elastic ^{1}H(e, e, p) reaction. After correcting for energy losses in the target along with internal bremsstrahlung for the incident electron, one can relate the beam energy to the electron scattering angle and the proton emission angle relative to the beam. By making several such measurements over a range of spectrometer angles at a fixed and independently measured beam energy, one arrives at a set of equations, each equation involving only the particle angles. Under the assumption that the angles are correctly measured except for a possible overall offset for each spectrometer (common to all kinematics within the set), one can determine these absolute offsets through a maximum likelihood analysis. The details of the method of extracting the spectrometer angular offsets can be found in Ref. [89]. In April of 2000 the first of such a series of ^{1}H(e, e′p) measurements was made. Several additional scans were made subsequently in order to assess the stability of the spectrometer angular offsets over time. To date, the first three scans have been analyzed [89,90], though the third lacked a direct, independent measurement of the beam energy. Based on the average of these three scans, the angular offsets were found to be -0.91 ± 0.08 mrad and -0.40 ± 0.07 mrad for the HRS-L and HRS-R arm, respectively. These averages were obtained by fitting only the angular offsets for the first two scans, constraining the beam energy to the values measured via the Arc method, and fitting both the angular offsets and the beam energy for the third scan. The error was estimated from the spread in survey results.

9.4. Absolute momentum determination

The relative momentum δ for an event measured by the spectrometer is used to calculate the absolute momentum p for that event:

$$p = p_0(1 + \delta) \tag{34}$$

where p_0 is the central momentum of the spectrometer, related to the dipole magnetic field B_0 by,

$$p_0 = \Sigma_{i=1}^{3} \Gamma_i B_0^i \tag{35}$$

where Γ_i are the spectrometer constants. The extraction of the spectrometer constants for the HRS pair is described in detail in Ref. [91].

At beam energies below 1.5 GeV, elastically scattered electrons from a thin ^{12}C target were used to calculate the spectrometer constant for each spectrometer. For the ground state of ^{12}C, the scattered electron momentum p is related to the beam energy E_i by

$$p = E_f = \frac{E_i - E_{\mathrm{loss1}}}{1 + 2E_i \sin^2(\theta/2)/M_{\mathrm{t}}} - E_{\mathrm{loss2}} \tag{36}$$

where E_f denotes the energy of the scattered electrons, M_t the mass of the target nucleus, and E_{loss1} and E_{loss2} the energy loss before and after scattering.

At higher beam energies the cross section for elastic scattering from ^{12}C vanishes, making it impossible to use the above method to calculate spectrometer constants. Instead, missing-energy measurements of the $1p_{1/2}$ state in the ^{12}C(e, e′p) reaction were used to calculate spectrometer constants for momenta above 1.5 GeV. For this method the kinematics were chosen such that one spectrometer momentum is set at the lower region where the constant has already been determined using the previous method, while the second spectrometer momentum is at the higher value where the constant needs to be determined.

Due to the relatively heavy mass of the ^{12}C nucleus, the spectrometer constant calculated using the above methods depends only weakly on the spectrometer angle. Furthermore, for a thin foil target the energy loss before and after

Table 6
The spectrometer constant coefficients for the HRS pair (see Eq. (35))

	Γ_1 (MeV/T)	Γ_2 (MeV/T^2)	Γ_3 (MeV/T^3)
HRS-L	2702 ± 1	0	-1.6 ± 0.4
HRS-R	2698 ± 1	0	-1.6 ± 0.4

scattering is relatively small and can be calculated accurately.

Spectrometer constants were thus determined with an accuracy of 4×10^{-4} over the full momentum range of both HRS. The beam energy for these measurements was measured using the Arc and eP methods to a few times 10^{-4}. In the 3 GeV region (where the Arc and eP results disagree) the spectrometer constants are fully consistent with the Arc results.

Table 6 lists the spectrometer constant coefficients for the HRS pair.

10. Summary

The main components—spectrometers, beam line, target systems and detector packages—of Hall A at JLab are described in detail. The beam line diagnostics provide accurate measurements of all relevant beam properties. A variety of target systems is available to cover a diverse research program. The optical properties of the two HRS magnetic spectrometers have been studied with the aid of the focal plane detector packages. The acceptance and resolution, both in momentum and angle, are close to the design parameters. After a brief commissioning period in May of 1997, the hall has operated reliably for a large set of experiments. In summary, the Hall A instrumentation has proven capable of supporting a broad research program, with an emphasis on very high luminosity and good momentum and angular resolution for a variety of reaction products.

Acknowledgements

The continuous dedicated and professional contributions from the Hall A technical staff and from the Accelerator Division is gratefully acknowledged. This work was supported by DOE contract DE-AC05-84ER40150 under which the Southeastern Universities Research Association (SURA) operates the Thomas Jefferson National Accelerator Facility, and by the National Science Foundation, the Department of Energy, the Istituto Nazionale di Fisica Nucleare (Italy), the Commissariat à l'Énergie Atomique (France), the Centre National de Recherche Scientifique (France), Conseil Régional d'Auvergne (France), the Natural Sciences and Engineering Research Council (Canada) and the Korean Science and Engineering Foundation.

References

[1] C.W. Leemann, D.R. Douglas, G.A. Krafft, Annu. Rev. Nucl. Part. Sci. 51 (2001) 413.
[2] B.A. Mecking, et al., Nucl. Instr. and Meth. A 503 (2003) 513.
[3] M.K. Jones, et al., Phys. Rev. Lett. 84 (2000) 1398.
[4] W. Xu, et al., Phys. Rev. Lett. 85 (2000) 2900.
[5] JLab experiment E93-050, P. Bertin, G. Fournier, spokespersons.
[6] JLab experiment E99-114, C. Hyde-Wright, A. Nathan, B. Wojtsekhowski, spokespersons.
[7] JLab experiment E91-011, S. Frullani, J. Kelly, A. Sarty, spokespersons.
[8] K.A. Aniol, et al., Phys. Lett. B 71 (2001) 959.
[9] P. Vernin, Research Program at CEBAF, Vol. II, 1986. p. 615.
[10] K.L. Brown, SLAC Report 75 (1970), revised edition, 1982, unpublished.
[11] The CEBAF Hall A Collaboration, Conceptual Design Report Experimental Equipment, A7 Detector Systems, 1990, unpublished.
[12] W.J. Schneider, et al., Adv. Cryogenic Eng. 41 (1996) 669.
[13] P. Vernin, et al., Nucl. Instr. and Meth. A 449 (2000) 505.
[14] K.A. Aniol, V. Punjabi, Hall A Line of Sight Shielding, JLab-TN-91-024, 1991.
[15] GEANT, Detector description and simulation tool, CERN Program Library W5013, wwwinfo.cern.ch/asd/geant/.
[16] G. Bathow, E. Freytag, K. Tesh, Nucl. Phys. B 2 (1967) 669.
[17] A.M. Boyarski, et al., C.2 yields of secondary particles from 18 GeV electrons, SLAC report, 1968.
[18] K.G. Fissum, et al., Nucl. Instr. and Meth. A 474 (2001) 108; Vertical drift chambers for the hall a high resolution spectrometers at Jefferson Lab, JLab-TN-00-016, 2000.
[19] J. LeRose, Report on studies of the effect on resolution of the exit window of the HRS spectrometers in Hall A, JLab-TN-00-001, 2000.

[20] M. Iodice, et al., Nucl. Instr. and Meth. A 411 (1998) 223.
[21] F. Garibaldi, et al., Lightweight mirrors for Cherenkov detectors, Nucl. Instr. and Meth., to be submitted.
[22] M. Shepherd, A. Pope, Investigation of BURLE 8854 photomultiplier tube, JLab-TN-97-028, 1997.
[23] A. Ketikyan, et al., Lead glass total absorption shower detector, hallaweb.jlab.org/equipment/detectors/detectors.html.
[24] E.J. Brash, et al., Nucl. Instr. and Meth. A 487 (2002) 346.
[25] M. Coman, M.S. Thesis, Florida International University, Miami (2000); B. Wojtsekhowski, et al., High performance threshold aerogel counters, Nucl. Instr. and Meth., to be submitted.
[26] R. Perrino, et al., Nucl. Instr. and Meth. A 457 (2001) 571.
[27] L. Lagamda, et al., Nucl. Instr. and Meth. A 471 (2001) 325.
[28] R. Iommi, et al., Test and Development of a Cherenkov diffusion detector prototype using Airglass aerogel at TJNAF, JLab-TN-00-010, 2000.
[29] V. Punjabi, et al., Phys. Rev. C, submitted for publication.
[30] O. Gayou, et al., Phys. Rev. C 64 (2001) 38202.
[31] M. Kmit, et al., Brookhaven Internal Report EP & S91-4.
[32] M. Berz, H.C. Hoffmann, H. Wollnik, Nucl. Instr. and Meth. A 258 (1987) 402.
[33] Hall A Operations Manual, hallaweb.jlab.org/document/OPMAN/.
[34] C.K. Sinclair, Design criteria for beam dumps for Halls A and C, JLab-TN-92-064, 1992.
[35] W. Barry, et al., Beam position measurement in the CEBAF recirculating linacs by use of pseudorandom pulse sequences, JLab-TN-90-246, 1990; Basic noise considerations for CEBAF beam position monitors, JLab-TN-91-087, 1991.
[36] R. Kazimi, et al., Proceedings of Particle Accelerator Conference, IEEE 0-7803-3503 (1996) 2610.
[37] K. Unser, IEEE Trans. Nucl. Sci. NS 28 (1981) 2344.
[38] J. Berthot, P. Vernin, Nucl. Phys. News 9 (1990) 12.
[39] D. Marchand, Ph.D. Thesis, University of Blaise Pascal, Clermont-Ferrand, 1997.
[40] O. Ravel, Ph.D. Thesis, University of Blaise Pascal, Clermont-Ferrand, 1997.
[41] A.A. Kresnin, L.N. Rozentsveig, Sov. Phys. JETP 5 (1957) 288.
[42] M. Baylac, et al., Phys. Lett. B 539 (2002) 8.
[43] D. Neyret, et al., Nucl. Instr. and Meth. A 443 (2000) 231.
[44] J.P. Jorda, et al., Nucl. Instr. and Meth. A 412 (1998) 1; N. Falletto, et al., Nucl. Instr. and Meth. A 459 (2001) 412.
[45] S. Escoffier, Doctorate Thesis, University of Paris 7, Denis Diderot, 2001, hallaweb.jlab.org/compton/Documentation/Papers/index.php.
[46] hallaweb.jlab.org/equipment/targets/cryotargets/Halla_tgt.html.
[47] JLab Cryotarget System, Nucl. Instr. and Meth., to be submitted.
[48] M. Amarian, et al., Phys. Rev. Lett. 89 (2002) 242301.
[49] JLab experiment E99-117, J.-P. Chen, Z.-E. Meziani, P. Souder, spokespersons.
[50] JLab experiment E97-103, T. Averett, W. Korsch, spokespersons.
[51] JLab experiment E97-110, G. Cates, J.-P. Chen, F. Garibaldi, spokespersons.
[52] JLab experiment E01-012, J.-P. Chen, S. Choi, N. Liyanage, spokespersons.
[53] L.S. Cardman, et al. (Eds.), The Science Driving the 12 GeV Upgrade of CEBAF, White Paper prepared for the NSAC Long Range Plan, www.jlab.org/div_dept/physics_division/GeV/WhitePaper_V11.pdf.
[54] M.A. Bouchiat, T.R. Carver, C.M. Varnum, Phys. Rev. Lett. 5 (1960) 373;
N.D. Bhaskar, W. Happer, T. McClelland, Phys. Rev. Lett. 49 (1982) 25;
W. Happer, et al., Phys. Rev. A 29 (1984) 3092.
[55] P.L. Anthony, et al., Phys. Rev. Lett. 71 (1993) 959.
[56] www.portplastics.com/plastics/high_perform/torlon.html.
[57] T.E. Chupp, et al., Phys. Rev. C 36 (1987) 2244.
[58] K.P. Coulter, et al., Nucl. Instr. and Meth. A 276 (1989) 29.
[59] N.R. Newbury, et al., Phys. Rev. A 48 (1993) 4411.
[60] G.D. Cates, et al., Phys. Rev. A 38 (1988) 5092.
[61] A. Abragam, Principles of Nuclear Magnetism, Oxford University Press, New York, 1961.
[62] S. Jensen, Ph.D. Thesis, Caltech, 2000; I. Kominis, Ph.D. Thesis, Princeton University, 2000; Hall A polarized ^{3}He collaboration, Nucl. Instr. and Meth., in preparation; www.jlab.org/e94010.
[63] N. Voegler, et al., Nucl. Instr. and Meth. 198 (1982) 293.
[64] F. Garibaldi, et al., Nucl. Instr. and Meth. A 314 (1992) 1.
[65] J. Gao, et al., Phys. Rev. Lett. 84 (2000) 3265;
N. Liyanage, et al., Phys. Rev. Lett. 86 (2001) 5670.
[66] S. Malov, et al., Phys. Rev. C 62 (2000) 057302.
[67] JLab experiment E00-102, A. Saha, W. Bertozzi, L.B. Weinstein, K.G. Fissum, spokespersons.
[68] JLab experiment E94-107, F. Garibaldi, et al., spokespersons.
[69] E. Cisbani, et al., A waterfall target system for Hall A at Jefferson Lab, INFN/ISS 97/04.
[70] A list of projects using EPICS can be found at csg.lbl.gov/EPICS/EPICS_Sites.html.
[71] Documentation on the MVME162 can be found at www.mcg.mot.com.
[72] Tool Command Language, www.tcl.tk.
[73] W.A. Watson, et al., CODA: a scalable, distributed data acquisition system, in: Proceedings of the Real Time 1993 Conference, p. 296; G. Heyes, et al., The CEBAF on-line data acquisition System, in: Proceedings of the CHEP Conference, 1994, p. 122; G. Heyes, et al., Real-time front end software for CODA, in: Proceedings of the real time 1993 Conference, p. 382; D.J. Abbott, et al., CODA Performance in the real world, 11th IEEE NPSS Real Time 1999 Conference, JLab-TN-99-12, 1999.
[74] E. Jastrzembski, et al., The Jefferson Lab trigger supervisor system, 11th IEEE NPSS Real Time 1999 Conference, JLab-TN-99-13, 1999.

[75] Physics Analysis Workstation, wwwasd.web.cern.ch/wwwasd/paw/.
[76] R. Brun, F. Rademakers, ROOT—an object-oriented data analysis framework, Proceedings of the AIHENP'96 Workshop, Lausanne, September 1996, Nucl. Instr. and Meth. A 389 (1997) 81.
[77] Jefferson Lab Scientific Computing Overview, cc.jlab.org/scicomp/overview/.
[78] E.A.J.M. Offerman, ESPACE User's Guide, hallaweb.jlab.org/espace/docs.html.
[79] CERN Program Library, wwwasd.web.cern.ch/wwwasd/cernlib.html.
[80] HBOOK—Statistical Analysis and Histogramming, CERN Program Library Long Writeup Y250, wwwasdoc.web.cern.ch/wwwasdoc/hbook/HBOOKMAIN.html.
[81] KUIP—Kit for a User Interface Package, wwwasdoc.web.cern.ch/wwwasdoc/kuip/kuipoverview.html.
[82] J.B. Mandeville, Ph.D. Thesis, University of Illinois at Urbana-Champaign, 1993.
[83] R.H. Wechsler, B.S. Thesis, Massachusetts Institute of Technology, 1996.
[84] garfield.web.cern.ch/garfield/.
[85] P.R. Bevington, Data reduction and error analysis for the physical sciences, McGraw-Hill, New York, 1969.
[86] The Hall A ROOT Project, hallaweb.jlab.org/root.
[87] hallaweb.jlab.org/root/optimize++.
[88] N. Liyanage, Optics calibration of the Hall a high-resolution spectrometers using the new C++ optimizer, JLab-TN-02-012, 2002.
[89] P.E. Ulmer, H. Ibrahim, N. Liyanage, Calibration of beam energy and spectrometer central angles using Hall A HRS in ^{1}H(e, e′p), JLab-TN-00-024, 2000.
[90] H. Ibrahim, P.E. Ulmer, N. Liyanage, Calibration of spectrometer central angles using Hall A HRS in ^{1}H(e, e′p), JLab-TN-02-032, 2002.
[91] N. Liyanage, Spectrometer constant determination for the Hall A HRS pair, JLab-TN-01-049, 2001.
[92] L.G. Levchuk, Nucl. Instr. and Meth. A 345 (1994) 496.